Moderate Reynolds number flow. Application to the human upper airways.

Annemie van Hirtum

Grenoble University, France

Moderate Reynolds number flow. Application to the human upper airways.

HABILITATION À DIRIGER DES RECHERCHES

Presented by

Annemie VAN HIRTUM

CNRS research fellow

30 June 2011

Jury

M. Xavier Pelorson, President
M. Jan-Bert Flor, Reviewer
M. Joël Gilbert, Reviewer
M. Jean-Christophe Valière, Reviewer
M. Avraham Hirschberg, Examinator
M. Pierre-Yves Lagrée, Examinator

Bestijg de trein nooit zonder uw valies met dromen,
dan vindt ge in elke stad behoorlijk onderkomen.

Zit rustig en geduldig naast het open raam:
gij zijt een reiziger en niemand kent uw naam.

Zoek in 't verleden weer uw frisse kinderogen,
kijk nonchalant en scherp, droomrig en opgetogen.

Al wat ge groeien ziet op 't zwarte voorjaarsland,
wees overtuigd: het werd alleen voor u geplant.

Laat handelsreizigers over de filmcensuur
hun woordje zeggen: God glimlacht en kiest zijn uur.

Groet minzaam de stationschefs achter hun groen hekken,
want zonder hun signaal zou nooit één trein vertrekken.

En als de trein niet voort wil, zeer ten detrimente
van uwe lust en hoop en zuurbetaalde centen,

Blijf kalm en open uw valies; put uit zijn voorraad
en ge ondervindt dat nooit een enkel uur te loor gaat.

En arriveert de trein in een vreemdsoortig oord,
waarvan ge in uw bestaan de naam nooit hebt gehoord,

Dan is het doel bereikt, dan leert gij eerst wat reizen
betekent voor de dolaards en de ware wijzen...

Wees vooral niet verbaasd dat, langs gewone bomen,
een doodgewone trein u voert naar 't hart van Rome.

Bericht aan de reizigers,
Jan van Nijlen (1934).

Thank you ...

The current document deals with research from 2004-2010 during which my main research activities correspond to the title of this document: “Moderate Reynolds number flow. Application to the human upper airways.”

Past, current and future results benefit from an important contribution of many persons. Thanks ! Arigato ! Merci ! Dank !

Grenoble, 2011
Annemie

Contents

Part I

Scientific summary

Chapter 1

Introduction

The study of fluid flow is an amasingly ordinary as well as fascinating subject. During the past few years I had the opportunity to work as a researcher in the field of *fluid flow modelling* applied to *airflow through the human upper airways* and related phenomena such as *speech production, ...* The current document is a brief report on the research to which I participated aiming a small contribution to this rich and stimulating research area.

Airflow through the human upper airways is due to physiological and anatomical properties characterised by velocities U and geometrical scales h which are, compared to airflows studied in other biofluids fields: *small* when dealing with *e.g.* aeronautics, geophysics or even cosmic flows and *large* when compared to dimensions and velocities encountered *e.g.* algae or bacterial biofluids. Consequently, typical Reynolds numbers $Re \propto Uh$ are of the order of magnitude of 10^3 which results in *moderate* Reynolds number flows.

Under certain conditions, quantitatively expressed by additional non-dimensional numbers related to *e.g.* unsteadiness or compressibility, flows characterised by moderate Reynolds numbers can be described by simplifications of the governing continuity and Navier-Stokes momentum equations as expressed by: boundary layer equations, self-similar solutions or an irrotational flow description. Besides the mentioned flow models, a start is made in order to account for turbulence as well as to formulate simple inverted flow models. It is intriguing to see how (relatively) complex problems can be simplified and represented within a simple formulation.

Besides flow modelling, qualitative as well as quantitative characterisation and validation of the flow field and related physical variables is required in order to determine the accuracy and relevance of the applied models and their dependence on input parameters, initial conditions *etc*. To this aim, several experimental setups and mechanical *in-vitro* replicas are used, improved or developed in order to study the flow field as well as related variables in a controlled and reproducible way. Although *in-vivo* observations of upper airway characteristics are the source of inspiration to build mechanical replicas, their actual design is a combination of additional factors: 1) it is aimed to reproduce experimentally the relevant range of non-dimensional numbers, 2) to facilitate accurate measurements with the sensors available in the experimental setup, 3) severe simplifications of the reality in order to study one particular feature, 4) limitations imposed by manufacturing *etc*. As a result, mechanical replicas might disappoint when expecting a duplicate of a portion of real life human upper airways. Nevertheless, simple replicas are more elegant since they allow to focus on a particular problem.

In addition to experimental validation, data are obtained from numerical simulation of the flow field. An one hand,

numerical data provide information of the flow field for which *in-vitro* data are difficult or impossible to be obtained. On the other hand, the outcome of numerical simulations can be validated on the experimental measurements.

Applications of airflow through the human upper airways, such as *speech production* or *obstructive sleep apnea*, are partly due to a fluid-structure interaction between airflow coming from the lungs and the upper airways tissues. Consequently, besides a flow model, a mechanical or/and acoustic model is required as well.

The topics outlined in this introduction are elaborated and illustrated in the following sections[1]. Finally, conclusions and perspectives are presented.

Good reading !

[1]Most relevant publications are mentionned.

Chapter 2

Fluid flow modelling

Based on the given orders of magnitude a dimensional analysis is performed. This yields a set of nondimensional numbers that can be interpreted as a measure of the importance of various flow effects from which several flow assumptions can be formulated [7, 87, 111].
Following the characteristic aspect ratio ($h/W << 1$) the flow is assumed to be characterised by a bidimensional (2D) flow description in the (x, y)-plane with h a typical minimum aperture and W a typical width. In case velocities are small compared with the speed of sound in air, so that the flow is assumed to be incompressible, i.e. squared Mach number $Ma^2 << 1$. Furthermore, for low Strouhal number ($Sr << 1$) the airflow is considered as primarily steady. Finally, as a first approximation, the flow is assumed to be inviscid considering characteristic Reynolds numbers ($Re_0 >> 1$).

2.1 Viscosity and flow separation

Although[1] it can be neglected for the bulk flow considering Reynolds numbers Re_0, the occurrence of flow separation due to viscosity strongly influences the flow development. Therefore, flow separation can not be neglected. In the studied flow models, the position of flow separation is determined either by an empirical *ad-hoc* assumption or predicted based on vanishing wall shear stress, $\tau(x)$=0, along the diverging portion of the wall where the flow is retarding, with

$$\tau(x) = \mu_0 \left(\frac{\partial u}{\partial y} \right)_{y=wall}, \tag{2.1}$$

and $u(x, y)$ the flow velocity within the boundary layer.

2.2 One-dimensional flow model with *ad-hoc* viscosity correction

Under[2] the assumptions of one-dimensional, laminar, fully inviscid, steady and incompressible flow, one-dimensional Bernoulli's equation can be used to estimate the pressure and velocity distribution within a constriction.

[1] Main publications: [103].
[2] Main publications: [19].

Bernoulli's equation is unable to account for flow separation and turbulent jet formation downstream of the minimum aperture h_M [96]. This phenomenon, resulting from very strong viscous pressure losses, must be taken into account in order to predict a pressure drop along the constriction from one-dimensional Bernoulli theory. Therefore an empirical criterion is required. The area associated with flow separation A_s is *ad-hoc* set to $A_s = cA_M$, i.e. $h_s = ch_M$ with $c \geq 1$ the separation coefficient, for the 2D geometry with area $A(x) = Wh(x)$ with the subindex M denoting the quantity at the position of minimum aperture. The pressure distribution along the flow direction $p(x)$ is then derived from the upstream pressure p_0 and the geometry $h(x)$ as,

$$p(x) = p_0 + \frac{1}{2}\rho\frac{\Phi^2}{W^2}\left(\frac{1}{h_0^2} - \frac{1}{h(x)^2}\right) \tag{2.2}$$

$$\Phi = A_s\sqrt{\frac{2p_0}{\rho}} \tag{2.3}$$

where p_0 is the upstream pressure, ρ the fluid density, Φ the volume flow rate and h_0 the upstream channel height before the constriction. The volume flow rate is assumed to be constant along the constriction, i.e. $\Phi = U(x)A(x) = U(x)Wh(x) = constant$. Accounting for $h_0 >> h_M$ and considering the pressure on the position of minimum aperture p_M results in:

$$p_M = p_0(1 - c^2) \tag{2.4}$$

Consequently, introducing an *ad-hoc* constant c determines both the position of flow separation as well as the maximum pressure drop. Note that for the one-dimensional theory the position of maximum pressure drop coincides with the position of minimum aperture. Eq. 2.4 can be used to estimate the constant c in order to match a measured pressure drop $p_0 - p_M$.
A quasi-one dimensional flow description is obtained when further accounting for viscous effects in case of small Reynolds numbers. Small Reynolds numbers appear for small apertures h_M. In order to account for viscosity, a Poiseuille term is added to eq. 2.2:

$$p(x) = p_0 + \frac{1}{2}\rho\frac{\Phi^2}{W^2}\left(\frac{1}{h_0^2} - \frac{1}{h(x)^2}\right) - 12\mu\frac{\Phi}{W}\int_0^x \frac{dx}{h(x)^3}. \tag{2.5}$$

The described flow model with the *ad-hoc* assumption of flow separation describes a movable flow separation position as a function of h_M for quasi-steady flow conditions, *i.e.* for low Strouhal numbers. Pressure differences induced by flow unsteadiness due to the fluctuations of $h(x,t)$, related to wall movements and/or upstream pressure $p_0(t)$, in time, are important for high frequency variations and/or wall vibrations involving collission. In this case, the additional pressure loss between positions $a < b$ due to the resulting unsteadiness in the volume airflow $\Phi(t)$ is expressed as:

$$\Delta P_U(a,b,t) = \frac{\rho}{W}\int_a^b \frac{d}{dt}\left(\frac{\Phi(t)}{h(x,t)}\right)dx. \tag{2.6}$$

Additional loss terms can be formulated based on geometrical considerations such as orifice, contraction or bending.

2.3 Boundary layer solution

In[3] the (quasi)-one-dimensional approach viscosity is either neglected (eq. 2.2) or corrected for with an additional Poiseuille term, assuming fully developed Poiseuille flow (eq. 2.5). However, at high Reynolds numbers Re_0, the

[3]Main publications: [103].

region in which viscous forces are important is confined to a thin layer adjacent to the wall, referred to as laminar boundary layer. Outside the boundary layer, the inviscid irrotational main flow, with velocity $U(x)$, is described by the one-dimensional flow equation 2.2. The resulting boundary layer theory is described by the Von Karman momentum integral equation for steady flows [87]. An approximated method to solve this equation for laminar, incompressible, bidimensional (x, y) boundary layers is given by Thwaites method [9,14,94]. Two shape parameters are introduced

$$H(\lambda) = \frac{\delta_1}{\delta_2} \tag{2.7}$$

$$S(\lambda) = \tau \frac{\delta_2}{U} \tag{2.8}$$

which are only functions of the velocity profile determined by the acceleration parameter $\lambda \approx \frac{dU}{dx}\delta_2^2$ with wall shear stress $\tau(x)$, displacement thickness δ_1,

$$\delta_1(x) = \int_0^\infty \left(1 - \frac{u(y)}{U}\right) dy, \tag{2.9}$$

and momentum thickness δ_2,

$$\delta_2(x) = \int_0^\infty \frac{u(y)}{U}\left(1 - \frac{u(y)}{U}\right) dy. \tag{2.10}$$

The Von Karman equation is then approximated by:

$$\delta_2^2(x)U^6(x) - \delta_2^2(0)U^6(0) \propto \int_0^\infty U^5(x)dx. \tag{2.11}$$

Eq. 2.11, in combination with the fitted formulas for $H(\lambda)$ and $S(\lambda)$ tabulated in [9], enables to compute the sought pressure distribution $p(x)$ up to the flow separation point x_s, where $\tau(x_s) = 0$, for a given input pressure and known geometry. Moreover, the point of flow separation x_s is numerically estimated, as separation is predicted to occur at $\lambda(x_s) = -0.0992$ [74]. Therefore no *ad-hoc* assumption needs to be made to account for flow separation, while the computational cost remains low.

2.4 Reduced Navier Stokes/Prandtl

A[4] second simplification of the Newtonian steady laminar incompressible bidimensional Navier Stokes equations is obtained making two additional assumptions [87]. Firstly the flow is assumed to be characterised by a large Reynolds number and secondly the geometrical transverse dimension (y-axis) is assumed to be small compared to the longitudinal dimension (x-axis). In the geometry under study the last assumption coincides with $h_0 << D$. Applying those assumptions to the bidimensional NS equations results in a system in which the transverse pressure variations are neglected. This system is referred to as the Reduced Navier Stokes/Prandtl (RNSP) system in accordance with Prandtl's formulation of the steady boundary-layer. Nondimensional variables are obtained by scaling u^* with U_0, v^* with U_0/Re, x^* with $h_0 Re$, y^* with h_0 and p^* with ρU_0^2 with the Reynolds number defined as $Re = U_0 h_0/\nu$. In terms of the nondimensional variables the resulting RNSP equations become:

$$\frac{\partial}{\partial x}u + \frac{\partial}{\partial y}v = 0, \qquad u\frac{\partial}{\partial x}u + v\frac{\partial}{\partial y}u = -\frac{\partial}{\partial x}p + \frac{\partial^2}{\partial y^2}u, \qquad 0 = -\frac{\partial}{\partial y}p. \tag{2.12}$$

[4]Main publications: [54, 110].

The no slip boundary condition is applied to the lower and upper wall. Since the lower wall of the geometry of interest corresponds to $y = 0$ and the distance to the upper wall is denoted with $h(x)$ the no slip condition becomes respectively ($u(x, y = 0) = 0$, $v(x, y = 0) = 0$) and ($u(x, y = h(x)) = 0$, $v(x, y = h(x)) = 0$). In order to numerically solve the RNSP equations the pressure at the entrance is set to zero and the first velocity profile need to be known (Poiseuille). There is no output condition.

2.5 Two-dimensional laminar Navier-Stokes

The[5] two-dimensional continuity and Navier-Stokes equations for steady, laminar and incompressible flow are:

$$\frac{\partial u_x}{\partial x} + \frac{\partial u_y}{\partial y} = 0, \tag{2.13}$$

$$\rho_0 \left(u_x \frac{\partial u_x}{\partial x} + u_y \frac{\partial u_x}{\partial y} \right) = -\frac{\partial p}{\partial x} + \mu \left(\frac{\partial^2 u_x}{\partial x^2} + \frac{\partial^2 u_x}{\partial y^2} \right), \tag{2.14}$$

$$\rho_0 \left(u_x \frac{\partial u_y}{\partial x} + u_y \frac{\partial u_y}{\partial y} \right) = -\frac{\partial p}{\partial y} + \mu \left(\frac{\partial^2 u_y}{\partial x^2} + \frac{\partial^2 u_y}{\partial y^2} \right), \tag{2.15}$$

where u_x and u_y denote the velocity component in the x and y dimension respectively [87]. For reasons of symmetry the upper half of the flow domain is discretised in finite elements and the commercial finite element software *ADINA CFD* is used as a solver [5]. The upstream pressure p_0 is applied at the inlet. The no-slip boundary condition is set to the rigid wall, while the symmetry centerline is treated as a slip wall. The mesh density is increased in the constriction in order to accurately predict flow separation by considering vanishing wall shear stress.

2.6 Large Eddy Simulation

The[6] airflow is simulated with Large Eddy Simulation (LES) for three dimensional incompressible unsteady flows [57, 84]. The spatially-filtered momentum equation (2.16) and continuity equation (2.17) are solved for a discretized flow domain,

$$\frac{\partial \bar{u}_i}{\partial t} + \frac{\partial}{\partial x_j} \left(\bar{u}_i \bar{u}_j \right) = -\frac{1}{\rho_0} \frac{\partial \bar{p}}{\partial x_i} + \nu \frac{\partial}{\partial x_j} \left(\frac{\partial \bar{u}_i}{\partial x_j} + \frac{\partial \bar{u}_j}{\partial x_i} \right) - \frac{\partial \tau_{ij}}{\partial x_j}, \tag{2.16}$$

$$\frac{\partial \bar{u}_i}{\partial x_j} = 0, \tag{2.17}$$

where $\bar{u}_i$ are the grid-scale velocity components ($i = 1, 2, 3$), $\bar{p}$ is the grid-scale static pressure and τ_{ij} is the subgrid scale (SGS) stress tensor. The physical parameters of the model are density ρ_0 and kinematic viscosity ν. A second-order Crank-Nicolson scheme (implicit method) is used for the discretization of the momentum equation. The unknowns $\bar{u}_i$ and $\bar{p}$ result from the decomposition of the velocity and the pressure into a resolvable ($\bar{u}_i$ and $\bar{p}$) and subgrid scale part (u_i' and p') as:

$$u_i = \bar{u}_i + u' \text{ and } p = \bar{p} + p'.$$

[5] Main publications: [20].
[6] Main publications: [108].

The SGS stress tensor τ_{ij} groups all terms which are not exclusively dependent on the large scale, so that:

$$\tau_{ij} = \bar{u}_i \bar{u}_j - \overline{u_i u_j}.$$

The subgrid scale turbulence is modelled with the Smagorinsky closure model, which is based on the formulation of the subgrid scale stress as:

$$\tau_{ij} - \frac{1}{3}\tau_{kk}\delta_{ij} = -2\nu_{SGS}\bar{S}_{ij},$$

with $\bar{S}_{ij}$ denoting the strain rate tensor and ν_{SGS} the subgrid scale eddy viscosity, which are defined by:

$$\bar{S}_{ij} = \frac{1}{2}\left(\frac{\partial \bar{u}_i}{\partial x_j} + \frac{\partial \bar{u}_j}{\partial x_j}\right) \text{ and } \nu_{SGS} = (C_S\Delta)^2\sqrt{2\bar{S}_{ij}\bar{S}_{ij}},$$

with Smagorinsky constant C_S. The size of the grid filter Δ is defined locally from the discretized volume as:

$$\Delta = \sqrt[3]{\text{Element Volume}}.$$

The Smagorinsky constant C_S is calculated locally in space and time using Lilly's least square procedure [34, 58]. The pressure field is computed from the velocity field using the fractional step method.

Chapter 3

Experimental conditions, measurement and nozzles

Accurate experimental data are important for two main reasons:

1. Experimental validation of modelled quantities under controlled and reproducible conditions
2. Qualitative and quantitative characterisation to increase understanding and to motivate the model approach

In order to realise accurate *in-vitro* experiments the following is needed:

1. A suitable experimental setup in order to measure the quantities of interest in an accurate and reproducible way
2. Mechanical replicas

The following section presents the range of flow conditions which are experimentally studied, some main aspects of experimental setup and measurements and finally the used nozzles and mechanical replicas are briefly presented.

3.1 Range of flow conditions

The studied range of flow conditions, in terms of non-dimensional numbers, should cover the range of interest to the human respiratory system. Consequently, the order of magnitude of human physiological quantities should be considered. Relevant geometrical and flow quantities for flow through the glottis and the oral tract and pertinent with respect to two typical phenomena such as phonation and obstructive sleep apnea (OSA) are summarised in Table 3.1.

So accounting for the properties of air the non-dimensional quantities are estimated and summarised in Table 3.2. From the resulting order of magnitude major flow assumptions can be formulated from which a modeling approach can be motivated.

Although estimation of the non-dimensional numbers of the flow allows to anticipate the flow behaviour, more information is needed in order to fully characterise the flow field. Therefore, qualitative as well as quantitative characterisation of the flow field is experimentally assessed.

Fluid properties of air		
ρ_0	Mean density	1.2kgm^{-3}
μ_0	Dynamic viscosity coefficient	1.5$\times$10^{-5}m^{2}s^{-1}
c_o	Speed of sound	350ms^{-1}
Oral tract		
L_o	Tongue length	50mm
L_t	Tract length	150-190mm
W_o	Pharyngeal width	15-25mm
H_o	Tract heigth	10-20mm
h_o	Minimum aperture	1-4mm
L_t	Length of teeth	1-2mm
D_o	Distance between teeth and lips	$1.7 \times L_t$
h_t	Minimum aperture at teeth	1-2mm
D_t	Distance between tongue constriction and teeth	5-15mm
U_o	Flow velocity	8ms^{-1}
f_o	Breathing frequency	0.25Hz
Glottis		
L_g	Glottal length	6-9mm
W_g	Glottal width	14-18mm
h_g	Glottal heigth	0-3mm
U_g	Flow velocity	10-40ms^{-1}
f_g	Fundamental frequency of oscillation	100-200Hz

Table 3.1: Some characteristic *in-vivo* geometrical and flow conditions for the glottis and the oral tract.

	oral tract	glottis	assumption
aspect ratio	$h_o/W_o << 1$	$h_g/W_g << 1$	two-dimensional
Ma^2	$10^{-4} << 1$	$10^{-2} << 1$	incompressible
Sr	$10^{-3} << 1$	$10^{-2} << 1$	steady
Re	$10^3 >> 1$	$10^3 >> 1$	inviscid

Table 3.2: Nondimensional numbers and flow assumptions: aspect ratio, Mach number Ma, Strouhal number Sr, Reynolds number Re.

3.2 Experimental setup and measurement

A general overview of the used experimental setups is schematised in Fig. 3.1.

The flow facility consists of compressed air (Copco GA7) circulating in a uniform tube with diameter 1cm for which the volume flow rate can be imposed by means of a pressure regulator (Norgren type 11-818- 987) and a manual valve. The valve controlled air supply is connected to a settling chamber of which the interior is tapered with acoustical foam (SE50AL-ML). The volume of the used settling chambers varies from 0.1 up to 0.8 m^3. Grids can be used in the settling chamber in order to reduce the turbulence intensity so that the measured streamwise turbulence intensity at the nozzle inlet is below 1%. A mechanical replica is mounted to the pressure tank. Different sensors can be added to the setup in order to measure relevant quantities such as pressure transducers (Kulite XCS-093), volume flow rate (TSI 4040) or hot-wire (TSI 1201-20) constant temperature anemometry (TSI IFA 300).

In complement to the experimental setup, different measurement aspects are developed as outlined in the following.

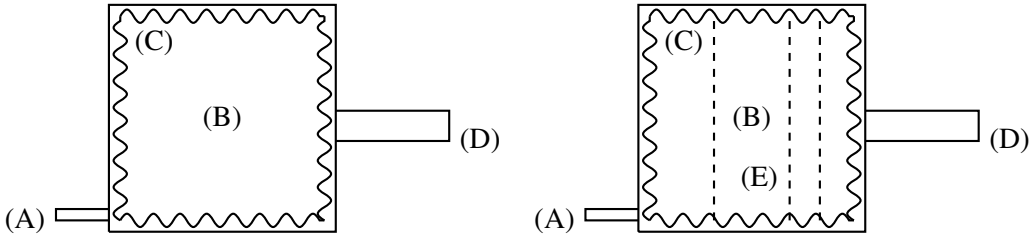

(a) without (b) with

Figure 3.1: General overview of experimental setup to wich sensors can be added: (A) supplied volume airflow rate, (B) settling chamber with (C) acoustical foam and (D) *in-vitro* replica. a) without and b) with air conditioning screens (E).

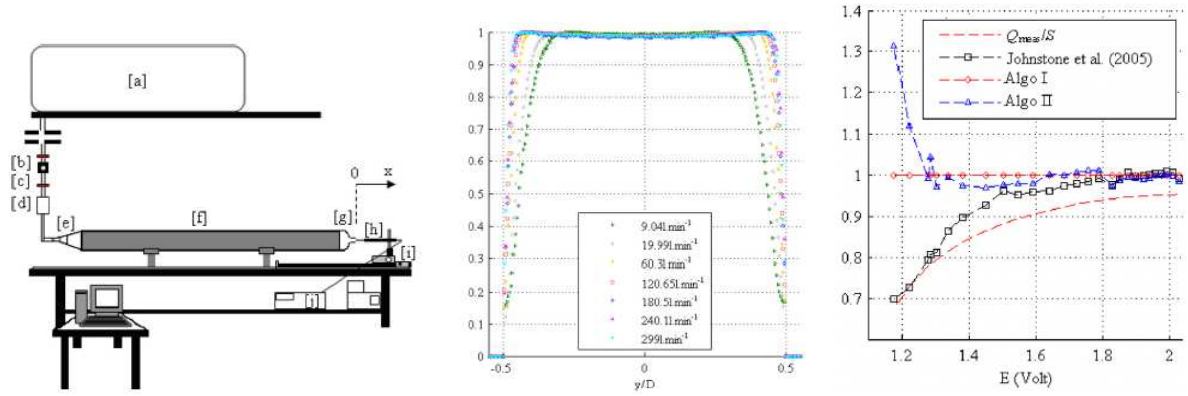

(a) (b) (c)

Figure 3.2: a) A sketch of the apparatus: (a) air supply, (b) pressure regulator, (c) valve, (d) mass flow meter, (e) divergent, (f) uniform pipe, (g) convergent nozzle, (h) hot film/wire, (i) positioning system, (j) IFA 300. b) Nozzle mean exit velocity profiles for seven volume flow rates. c) Overview of differences between four calibration methods: bulk velocity $U_{cal} = Q_{meas}/S$, Johnstone's method [50], Algo I and Algo II.

3.2.1 Hot-wire/film calibration

With[1] respect to the development of the available measurement techniques and accounting for the aimed flow conditions a contribution is made to the development of a simple calibration algorithm for hot film/wire allowing a joint calibration for low ($< 2m/s$) and moderate ($> 2m/s$) flow velocities. The simple and inexpensive calibration setup and results are illustrated in Fig. 3.2 [39].

Two simple calibration algorithms are proposed taking into account the development of the boundary layer. Algo I uses an estimation of the displacement thickness δ_1 from the measured mean velocity profile across the nozzle exit. Algo II estimates the displacement thickness by making additional assumptions on the velocity profile in the boundary layer and its thickness δ. As a benchmark comparison is made with the optimisation method proposed in [50] and an estimation of the bulk velocity. Comparison of the different approaches is summarised in Table 3.3 and illustrated in Fig. 3.2.

Algo I is the most accurate since the displacement thickness δ_1 is calculated from the mean velocity profile and

[1]Main publications: [39].

Procedure	Measurement	Velocity range	Major drawback	Major advantage
[50]	$U(y)$, Q_{meas}	$U_{cal} \geq$ 3m/s	accuracy loss with boundary layer development	simple to implement
Algo I	$U(y)$, Q_{meas} as [50]	$U_{cal} \geq 0.17$m/s	accurate spatial exit profile measurement	most accurate for low velocities
Algo II	Q_{meas}, U_c^0	$U_{cal} \geq 0.5$m/s	ad-hoc coefficient	reduced number velocity data

Table 3.3: Overview of assessed hot film/wire calibration methods with exit velocity profile $U(y)$, centerline velocity at the nozzle exit U_c^0 and measured volume flow velocity Q_{meas}.

no further assumptions are made. Therefore, the lower velocity limit of Algo I is mainly dictated by measurement errors. The lower limit of Algo II on the other hand is dictated by the failure of the assumption of the linear growth profile in the boundary layer. Finally, Johnstone's method is limited by the development of the boundary layer itself.

3.2.2 Smoke visualisation

In[2] complement to the pointwise spatial information of the flow field by anemometry, flow visualisation methods are of interest to obtain a global overview of the flow field. The experimental setup is illustrated in Fig. 3.3.

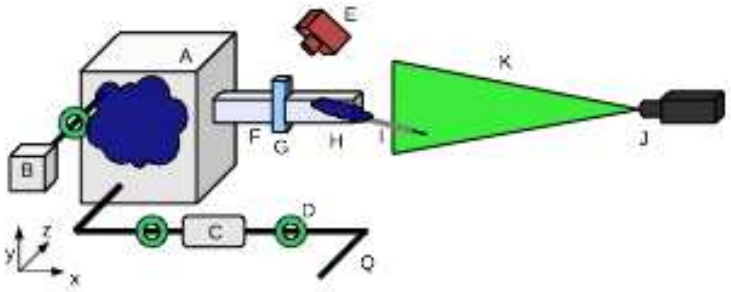

Figure 3.3: Schematic overview of smoke visualisation setup: settling chamber (A), smoke generator and injector for settling chamber (B), volume airflow rate supply (Q), pressure regulator and thermal mass flow meter (C), manual valves (D), laser source (J), camera (E) perpendicular to the two-dimensional laser sheet (K), manual gate (G) with attachment tube (H), nozzle (M), alternative incense burning (I). The two-dimensional illumination coincides with the plane $z = W/2$ and the x-axes indicates the main flow direction.

In order to realise smoke visualisation the nozzle or mechanical replica under study is attached to a settling chamber with volume 0.112m^3. Neutrally buoyant white smoke (Steinigke Showtechnic GmbH, fluid smoke, polyglycol, glycerol, 3-ethyleenglycol, 1.2 propyleneglycol in water double distilled water, 1.06g/cm^3) is injected in the settling chamber by means of a fog machine (Kool Light, FOG-1200E, 1200W, maximum volume flow rate 300m^3/min) up to a manual valve. Alternatively, incense is used to fill the nozzle downstream the settling chamber downstream a closed manual gate. In both cases smoke is added in absence of airflow. Airflow is applied once sufficient smoke is

[2]Main publications: [37, 106].

injected.

Two-dimensional illumination is applied with a laser light beam. A a two-dimensional laser light beam is generated by a class IIIb laser light source (Laserglow Technologies, LRS-0532-TFM-00200-10, 234.2mW, wavelength of 532nm and with spectral line width < 0.1nm) to which a 10 degree cylindrical lens is added. The resulting beam has an aperture diameter of 1mm with a divergence angle < 1.5mrad.

To record the illuminated smoke pattern, a color camera (Casio, EXILIM Pro EX-F1, 6.0 million effective pixels and a 12X optical zoom) was positioned perpendicular to the laser sheet. The back wall of the test chamber was painted in black to ensure a good contrast with the smoke pattern. Movies are recorded at typically 300fps. So, the time interval between consecutive images is 3.3ms. The digitised two-dimensional images are typically 512×384 data matrices. Spatial calibration of the images is performed.

3.2.3 Acoustic insulation box

Aero-acoustic[3] experiments are performed in an ordinary laboratory room equipped with a flow facility consisting of compressed air circulating in a uniform tube with diameter 1cm for which the volume flow rate can be imposed by means of a pressure regulator (Norgren type 11-818-987) and a manual valve. The compressor is isolated in a separated room. The presence of the pressure regulator and airflow circuit in the room is a source of constant broadband background noise, which can not be filtered out with standard techniques since it affects all frequencies. Additional constant noise sources are due to the experimental procedure such as computers ventilation noise during data acquisition. Besides unwanted noise sources inherent to the airflow facility or experimental procedure, several punctual and random unwanted noise sources are related to inside activities of colleagues or outdoor activities of passengers or traffic. Consequently, instead of isolating individual noise sources it has been chosen to integrate a non expensive experimental box in the ordinary room which serves as an insulation room.

The box is inserted in the ordinary room with no acoustical treatment of volume 49.8m^3 and dimensions $4.45 \times 4 \times 2.80$m, length $\times$ width $\times$ height. Due to the location of windows, entrance door, space required for experimental material and instruments (such as the settling chamber for flow experiments) and manufacturing issues, the external dimensions of the box are reduced to $2.07 \times 2.10 \times 2.14$m, length $\times$ width $\times$ height. A two-dimensional spatial overview of the ordinary room with insulation box is given in Fig. 3.4(a).

The insulation box is built in rigid flat wooden fiber board insulation panels with thickness 2.5cm to which acoustic foam (SE50-AL-ML, Elastomeres Solutions) with thickness 5cm is added. The foam absorbs frequencies in the range from 100 up to 10kHz which is 'a-priori' suitable for broadband noise sources such as pressure regulator, PC ventilator, etc. The efficiency of the acoustic foam depends on the noise frequencies. Absorption and attenuation of frequencies below 1000Hz are improved thanks to the inclusion of a basis-layer of PVC (Polyvinyl chloride 5kg/m^2) to which PU Ether (Polyurethane) foam is added. Therefore, the final insulation panels of the insulation box are three-layered - wood, PVC, foam - with a total thickness of 7.5cm as illustrated in Fig. 3.4(b). Characteristics of the insulation box are summarised in Table 3.4.

[3]Main publications: [29, 105].

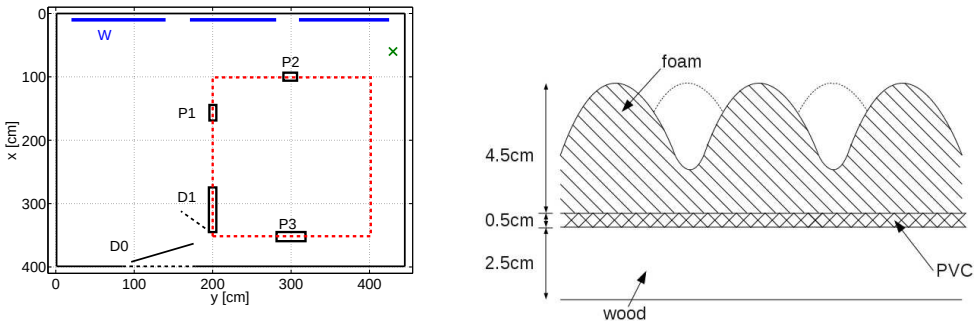

(a) room overview (b) panel section

Figure 3.4: a) Two-dimensional spatial overview of experimental room without acoustical treatment with entrance $D0$, room windows W, compressed air supply $\times$, insulation box (dashed rectangle) equipped with 3 trapdoors P and door access $D1$. b) Illustration of a section of the three-layered insulation panel.

	Values & range	
Internal dimensions	L_x=1.92m, L_y=1.95m, L_z=1.99m	
Internal volume V	$7.45m^3$	
Internal wall surface S	$22.9m^2$	
Absorbing foam (Elastomeres Solutions) (SE50-AL-ML)	98% ($\alpha_f = 0.98$) 80% ($\alpha_f = 0.8$) <80% ($\alpha_f \leq 0.8$) (linear increase)	$2500 < F < 10000$Hz $1000 < F < 2500$Hz $100 < F < 1000$Hz
Wall thickness	7.5cm	

Table 3.4: Relevant insulation box characteristics. Internal dimensions correspond to length L_x $\times$ width L_y $\times$ height L_z. Corresponding values of the absorption coefficient of the foam α_f for different frequency ranges are indicated [1].

Three trapdoors allow access for instrumentation cables. In addition, trapdoors can be used to insert the nozzle to be studied. Trapdoors are made of the same rigid wood panels as the box and have internal dimensions 20 $\times$ 20cm, 20 $\times$ 20cm and 70 $\times$ 70cm. The trapdoors are placed at middle panel height and their positions are indicated in Fig. 3.4(a). A wooden access door of internal dimensions 70 $\times$ 200cm (width $\times$ length) and thickness 4.5cm, is installed to allow access inside the box for setting up the instrumentation. Acoustic foam is added to trapdoors and access door as well. Besides insulation from outdoor noise sources, the presence of acoustic foam intends to avoid acoustic volume resonance frequencies which depend inversely upon the characteristic lengths of the resonating volume, indicated $L_{x,y,z}$ in Table 3.4. Finally, note that, if required, the whole structure can be dismounted and remounted.

The acoustic performance is firstly evaluated with respect to unwanted noise sources which are inherent to the measurement procedure and to the flow facility. Signals are high-passed filtered with a fifth order Butterworth filter with cutoff frequency 100Hz, so that the electrical network frequency of 50Hz and low frequency noises are excluded. In addition, attenuation below 100Hz is expected to be insufficient due to the poor attenuation of the foam as indicated in Table 3.4. All sound pressure levels are expressed in dB SPL as:

$$SPL = 20log_{10}\left(\frac{p_{rms}}{p_{ref}}\right), \tag{3.1}$$

where $p_{ref} = 2.10^{-5}$Pa and $p_{rms} = \sqrt{\frac{1}{N}\sum_{i=1}^{N} p_i^2}$, with p_i the i^{th} instantaneous acoustic pressure. Sound pressure is measured by omni directional microphones Bruel & Kjaer (type 4192) with associated pre-amplifier (B&K 4165) and additional amplifier ($0 \leq G \leq 50$dB) and power supply (B&K 5935L) is used to perform sound measurements in the untreated room and in the insulation box. Sounds are recorded during 10s consecutively for steady sources at 2^{16} samples per second. The sensitivity of the microphone is determined with a calibrator (B&K4231).

The attenuation of external noise sources is quantified using a simple additive model for the sound pressure level so that an unwanted source is considered to have no influence in case the difference between wanted and unwanted source ΔdB is more than 25dB.

The attenuation of background noises measured inside and outside the insulation box due to airflow supply (180l/min and 110l/min) and PC usage is given in Table. 3.5. In addition, the attenuation of human conversational speech is

	Measured SPL levels		
Noise	Non-treated room (SPL_R)	Insulation box (SPL_I)	Attenuation (SPL_R - SPL_I)
180l/min	92dB	36dB	>25dB
110l/min	82dB	36dB	>25dB
PC	68dB	37dB	>25dB
Voice	70dB	38dB	>25dB
Reference level	36dB		

Table 3.5: Performance of the insulation box for typical background noise due to the measurement procedure: measured sound pressure levels (SPL) for air supply (180 and 110l/min) and PC usage in the non treated room (R) and in the insulation box (I).

shown. SPL-values measured in the non treated room are > 80dB for airflow supply, 68dB for computer usage and 70dB for the voice sample. Recall that the SPL level of the voice sample is within the range expected for human conversational speech [80]. The value of computer usage and voice are from the same order of magnitude whereas the SPL values measured for airflow supply are > 10dB larger, so that airflow supply is the most important source of background noise during the measurements. From Table 3.5 is observed that corresponding attenuated values measured in the insulation box approximate the reference level of 36dB. In addition, it is seen that all background noise sources are attenuated with more than 25dB. Consequently, the attenuation of SPL for unwanted noise sources inherent to the measurement procedure and airflow supply is satisfactory.

Next, the spectral attenuation of the insulation box is considered. Fig. 3.5(a) illustrates the attenuation with respect to the reference level for unwanted noise sources inherent to the experimental procedure, *i.e.* airflow supply 110l/min and PC usage. Both sources are broadband noises for which the spectrum covers the entire frequency domain when measured in the non treated room. It is observed that the corresponding spectra measured inside the insulation box match the reference level for $f \geq 300$Hz and that for $f < 300$Hz the difference with the reference level is less than 10dB. Note that despite the approximately square shape of the insulation box, the attenuation is independent of its acoustical modes. Consequently, as for the attenuation in SPL, the spectral attenuation of the insulation box for unwanted noise sources inherent to the measurement procedure and airflow supply is satisfying.

The homogeneity of measured dB SPL is estimated to have an accuracy of 4% for all frequencies in the interval 100Hz up to 10kHz. An averaged absorption coefficient α is estimated from matching modelled and measured decay behaviour of a point source to be $0.8 \leq \alpha \leq 0.95$ which is in the characteristic range of the foam. From the measured and modelled reverberation times Tr, it is observed that the insulation box is characterised by a short

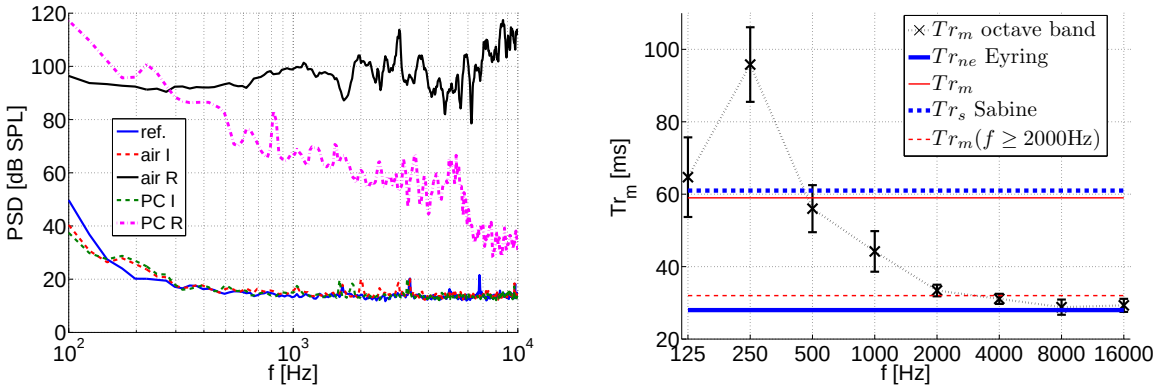

(a) (b)

Figure 3.5: a) Performance of the insulation box for typical background noises due to the measurement procedure: Power Spectral Density (PSD) for 110l/min air supply and PC usage in the non treated room (R) and in the insulation box (I). b) Estimated mean ($\times$) and standard deviation (vertical error bars) of the reverberation time Tr_m for each octave band in the range from 89Hz up to 22.5kHz. The center frequency of each band is indicated. For comparison also the averaged measured Tr_m (thin full line), the averaged high-pass filtered $Tr_m(f \geq 2000)$ (thin dashed line), modelled from Sabine's equation Tr_s (thick dashed line) and modelled from Norris-Eyring equation Tr_{ne} (thick full line) are indicated.

reverberation time in the range $30 \leq Tr \leq 60$ms, which can be approximated by a constant value $Tr \approx 31 \pm 2$ms for frequencies $f \geq 1400$Hz as illustrated in Fig. 3.5(b).

3.3 Nozzles and mechanical replicas

Rigid and deformable nozzles and mechanical replicas with different degrees of complexity are designed to study the flow and the influence of initial conditions on the flow development as well as the sound produced. In the following an overview is given of the used geometries.

3.3.1 Rigid axisymmetrical nozzles

Convergent axisymmetrical nozzle

A[4] convergent axisymmetrical nozzle is obtained as two matched cubics. The radius $R(x)$ of the resulting parameterised axisymmetrical nozzle is defined as:

$$R(x) = \left(\frac{D_1}{2} - \frac{D_2}{2}\right)\left(1 - \frac{(x/L)^3}{(x_m/L)^2}\right) + \frac{D_2}{2}, \qquad x \leq x_m \tag{3.2}$$

$$R(x) = \left(\frac{D_1}{2} - \frac{D_2}{2}\right)\frac{(1-x/L)^3}{(1-x_m/L)^2} + \frac{D_2}{2}, \qquad x > x_m \tag{3.3}$$

[4]Main publications: [30, 39].

with x the main streamwise direction, matching point $x = x_m$, inlet diameter D_1, outlet diameter D_2 and total nozzle length L. Consequently, the varying nozzle's geometry with diameter $D(x)$ is defined from the parameter set (D_1, D_2, L, x_m) or alternatively $(D_{1,2}, CR, L, x_m)$ since CR denotes the area contraction ratio defined as $CR = (D_2/D_1)^2$. The resulting nozzle geometry is illustrated in Fig. 3.6.

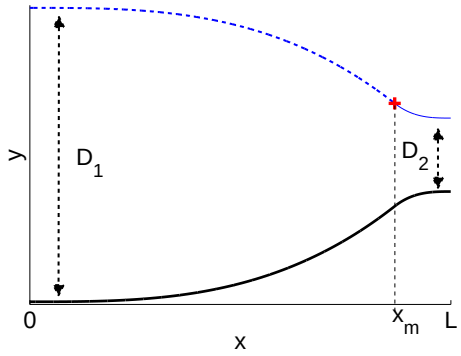

Figure 3.6: Illustration of parameterised axisymmetrical nozzle geometry, $D(x) = 2R(x)$, obtained from matching at $x = x_m$ an upstream cubic (3.2) (dashed line) and a downstream cubic (3.3) (thin full line) with parameters D_1=100mm, D_2=25mm, L=60mm and x_m=52mm. The longitudinal x-axis corresponds to the main streamwise direction and the y-axis to the transverse direction.

Extended convergent-divergent nozzle

An[5] extended convergent-divergent axisymmetrical nozzle is composed of a diffuser coupled to a uniform circular extension tube with fixed diameter $d = 25$mm and varying length L_t. The diffuser has a 14^o convergent portion of length 2cm followed by a 22^o divergent portion of length 5cm. The ratio of outlet and minimum diameter yields 5. The outlet diameter of the diffuser equals the extension tube diameter d. The assessed extension tube lengths yield 1, 3, 9, 18 and 50cm corresponding to length-to-diameter ratio $L_t/d \in \{0.4, 1.2, 3.6, 7.2, 20\}$. The geometry of diffuser and downstream extension tube is schematically detailed in Fig. 3.7.

Extended sharp contraction nozzle

An[6] extended axisymmetrical sharp contraction nozzle is obtained by coupling a uniform circular extension tube with fixed diameter $d = 25$mm and varying length L_t directly to the settling chamber. This way the airflow sustains a brutal contraction equal to 80:1 from the settling chamber to the pipe. The assessed extension tube lengths yield 3, 11, 18, 50 and 133cm corresponding to a length-to-diameter ratio $L_t/d \in \{1.2, 2.2, 4.4, 7.2, 20, 53.2\}$. The geometry of diffuser and downstream extension tube is schematically detailed in Fig. 3.8.

[5] Main publications: [35, 107].
[6] Main publications: [35, 36].

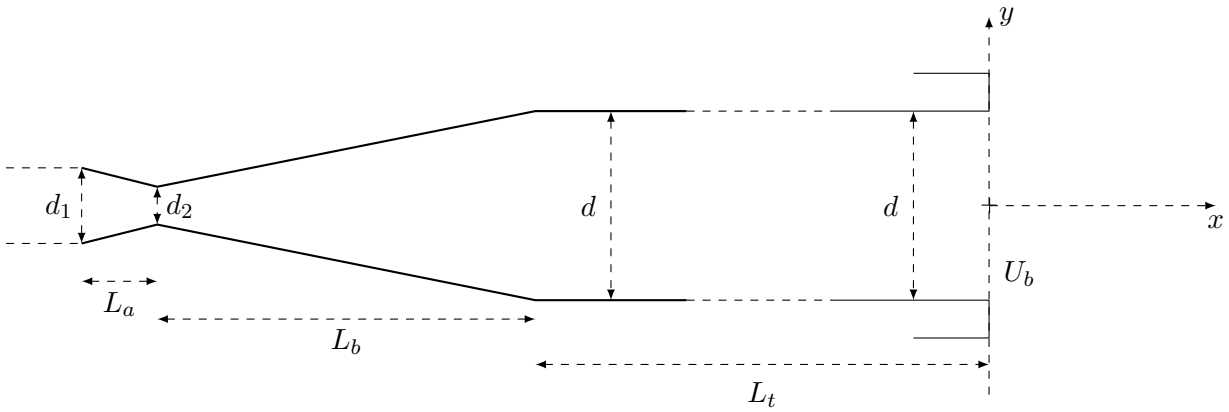

Figure 3.7: Schematic overview of the diffuser geometry (d_1=1cm, d_2=0.5cm, L_a=2cm, L_b=5cm) and extension tube of variable length $L_t \in \{1, 3, 9, 18, 50\}$cm and fixed diameter d=2.5cm so that $L_t/D \in \{0.4, 1.2, 3.6, 7.2, 20\}$. The x dimension follows the centerline of the tube in the flow direction and y corresponds to the transverse direction.

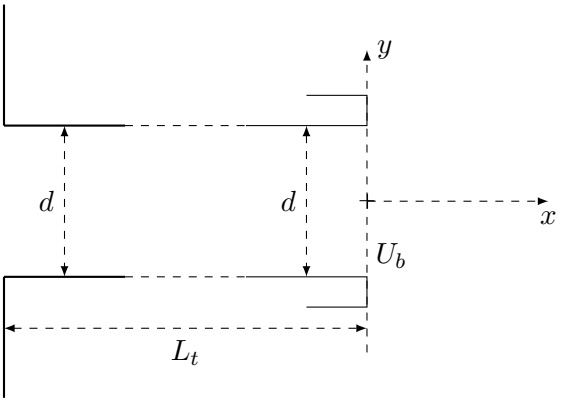

Figure 3.8: Schematic overview of the sharp 90^o contraction geometry of contraction degree and extension tube of variable length $L_t \in \{3, 11, 18, 50, 133\}$cm and fixed diameter d=2.5cm so that $L_t/D \in \{1.2, 2.2, 4.4, 7.2, 20, 53.2\}$. The x dimension follows the centerline of the tube in the flow direction and y corresponds to the transverse direction.

3.3.2 Rigid rectangular nozzles

Rectangular nozzle with 1 sharp obstacle

The[7] nozzle consists of a sharp obstacle inserted perpendicular in a rectangular channel as schematically depicted in Fig. 3.9. The uniform channel has width $w_1 = 105$mm, unconstricted channel height $h = 25$mm and a typical total length $l_{noz} = 360$mm. The obstacle consists of a trapezoidal wedge defined by, respectively, its base $l_{pal} = 6.6$mm, tip length $l_t = 1.25$mm and height $h_t = 17.5$mm. Consequently, when inserting the obstacle in the unconstricted channel, the leading and trailing angles of the obstacle with the upper plane of the rectangular channel are $\theta_1 = 107°$ and $\theta_2 = 90°$. Next, the obstacle is inserted at a distance $l_0 = 11$mm upstream of the nozzle outlet. The resulting minimum aperture at the obstacle yields $h = h_0 - h_t = 7.5$mm.

The aspect ratios of the nozzle, both in the unconstricted and constricted region, are superior to 1, $w_1/h_0 \approx 4$ and $w_1/h \approx 15$. Consequently, the flow is expected to be statistically similar to a two-dimensional flow. This assump-

[7]Main publications: [35, 108].

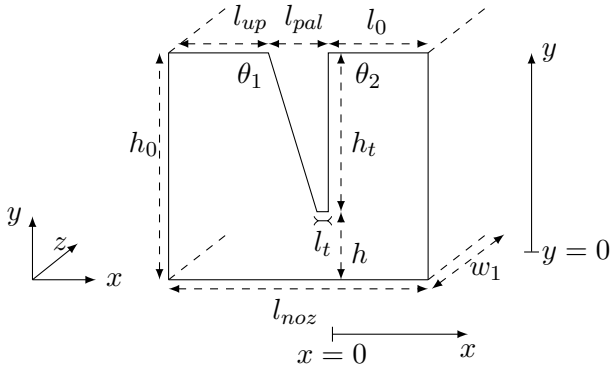

Figure 3.9: Schematic representation of the nozzle. The x-axis corresponds to the main flow direction and the y-axis to the transverse direction perpendicular to the flat wall.

tion was experimentally verified by hot-film anemometry measurements. The contraction ratio h_0/h yields ≈ 3.3 resulting in a 70% obstruction degree at the obstacle. The ratios of 1) the obstacle length l_{pal} and 2) the channel downstream the constriction l_0 to the minimum aperture yield $l_{pal}/h = 0.88$ and $l_0/h = 1.47$.

Rectangular nozzle with 1 gradual and 1 sharp obstacle

The[8] rectangular nozzle with 1 gradual and 1 sharp obstacle is shown in Fig. 3.10. The rigid 'in-vitro' replica consists of two constrictions, C_1 and C_2, inserted in a uniform rectangular channel. The unconstricted channel has length $L_0 = 180$mm, height $h_0 = 16$mm, width $w = 21$mm and aspect ratio $w/h_0 = 1.3$. The shape of both constrictions C_1 and C_2 is fixed. Their lengths in the x-direction yield $l_1 = 30$mm for C_1 and $l_2 = 3$mm for C_2. The aperture h_1 is fixed to 3mm, which corresponds to a constriction degree of 81%. The distance of the trailing edge of C_2 to the channel exit, L_2, is fixed to 6mm. The distance of the trailing edge of C_1 with respect to the channel exit, L_1, can be varied as well as aperture height h_2 of constriction C_2. Therefore, besides the inlet height h_0, the pressure distribution is determined by the set of geometrical parameters $\{h_1, L_1, h_2\}$ among which L_1 and h_2 can be varied. In order to validate the pressure drop, three pressure taps are assessed at positions $p_0 = 30$mm, $p_1 = 160$mm and $p_2 = 173$mm from the channel inlet. The position of the pressure taps is fixed to prevent leakage.

Constriction shapes: fixed and movable

Two[9] sets of uniform and round constriction shapes are available as shown in Fig. 3.11(a). Constrictions are mounted by means of an adjustement screw in a rectangular holder of fixed width $w = 25$mm, illustrated in Fig. 3.11(b), to which side walls are added covering at least the constricted portion. Note that a downstream channel of varying length and geometry can be added. The adjustement screws allows to vary the minimum aperture h.

To each constriction of length 10mm a step motor (Radiospare L92121-P2) can be attached so that its movement along the y-axis can be controlled (LabView, National Instruments). A symmetrical oscillatory movement, $y(t) = A\sin(2\pi Ft)$, is imposed to both constrictions for which both frequency F and amplitude A can be varied.

[8] Main publications: [24, 101, 109].
[9] Main publications: [17, 19].

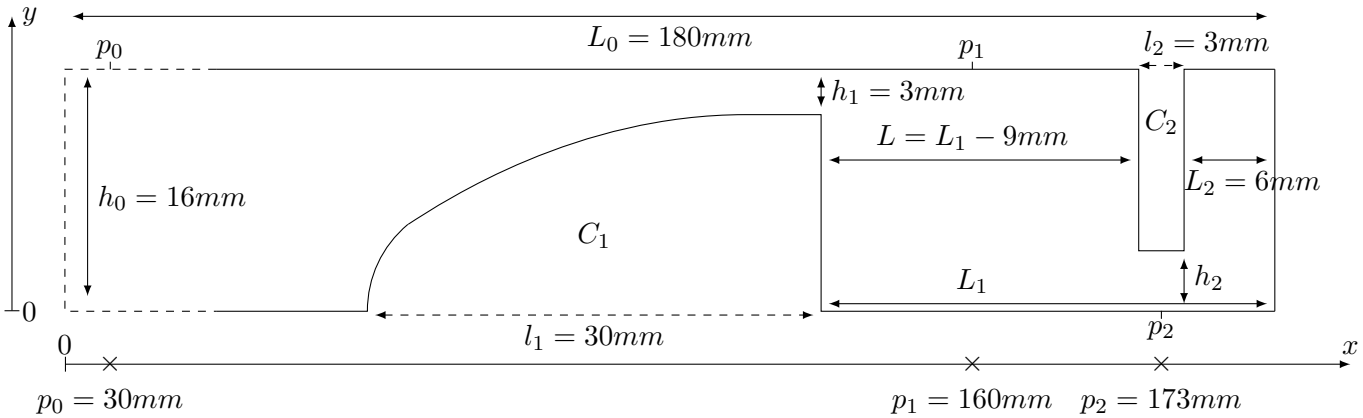

Figure 3.10: Two dimensional schema of rigid 'in-vitro' replica: rectangular channel with fixed unconstricted height $h_0 = 16$mm, uniform width $w = 21$mm and total length $L_0 = 180$mm containing two constrictions C_1 and C_2. The main streamwise direction corresponds to the x-axis. The constricted portions C_1 and C_2 has streamwise lengths $l_1 = 30$mm and $l_2 = 3$mm, respectively. The minimum aperture height of C_1 is indicated h_1 and of C_2 is denoted h_2. The distance between the channel exit and the trailing edge of C_1 and C_2 is denoted L_1 and L_2, respectively. The distance between the trailing edge of C_1 and the leading edge of C_2 is denoted L. The geometrical parameters yield $L_2 = 6$mm and $h_1 = 3$mm. The geometrical parameters L_1 and h_2 can be varied. Three pressure taps are present at downstream positions $p_0 = 30$mm, $p_1 = 160$mm and $p_2 = 173$mm.

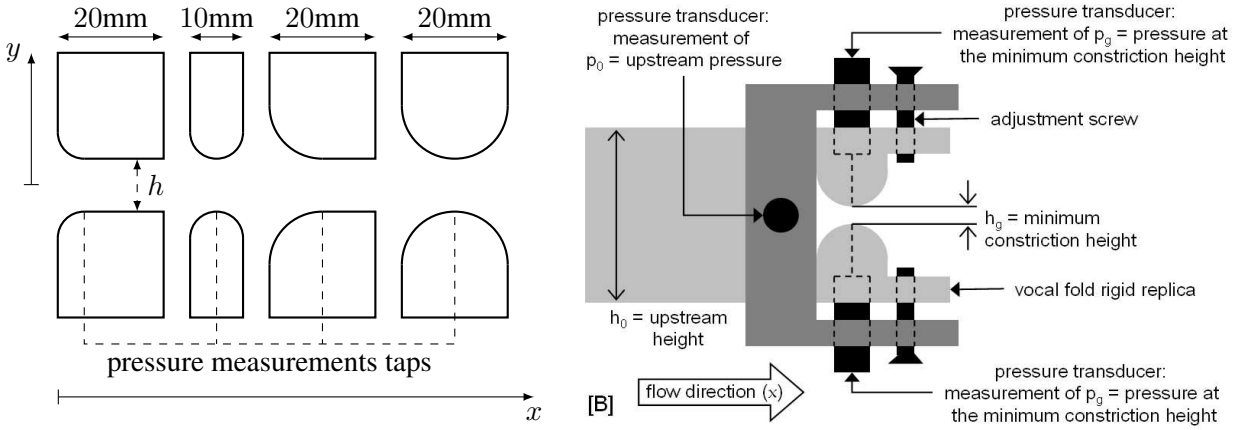

Figure 3.11: a) Different uniform (a,c) and round (b,d) constriction shapes with fixed width $w = 25$mm. b) Schematic representation of the rectangular constricted portion with variable heigth h.

Complete or partial closure can be realised as well as symmetrical or asymmetrical movement so that unsteady flow conditions due to a moving wall can be realised.

To one constriction shape of length 20mm a step motor (Radiospare L92121-P2) can be attached so that its movement along the y-axis is driven (LabView, National Instruments). An oscillatory movement, $y(t) = A\sin(2\pi Ft)$, is imposed for which both frequency F and amplitude A can be varied. Complete or partial closure can be realised. Asymmetrical movement is obtained so that unsteady flow conditions due to a moving wall can be realised. The driven movement and optical sensor to measure the time-varying aperture is described in [22].

Asymmetrical constriction

An[10] asymmetrical rectangular constriction is obtained by placing a rigid half cylinder with diameter $D = 49$mm inside a rectangular uniform pipe as shown in Fig. 3.12. The minimum aperture can be varied. Pressure taps are foreseen along the flat bottom plate of the constriction.

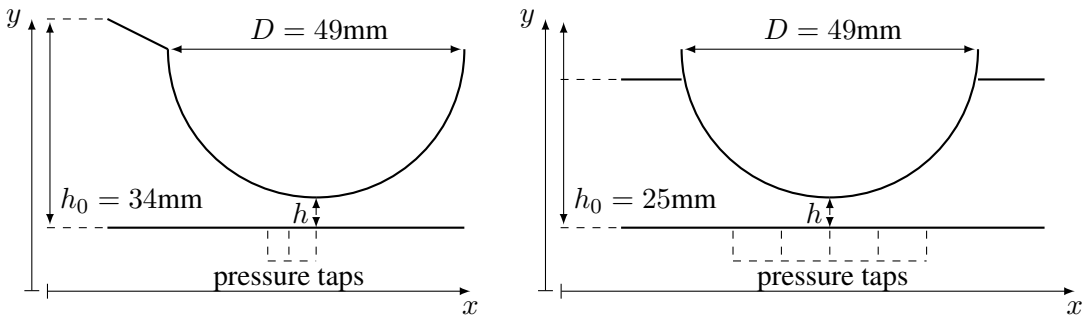

(a) (b)

Figure 3.12: Asymmetrical rigid nozzles a) fixed width $w = 34$mm and b) fixed width $w = 25$mm.

3.3.3 Deformable mechanical replicas

Deformable asymmetrical constriction

A[11] deformable asymmetrical constriction which can be schematically presented by Fig. 3.12(b) is obtained by replacing the rigid cylinder by a deformable portion. The deformable portion consists in a hollow cylinder which can be filled with water and covered with latex (Piercan Ltd) as illustrated in Fig. 3.13. Mechanical properties of the deformable portion are varied by changing the internal water pressure in the cylinder.

The transverse deformation of the mechanical replica due to the interaction with an upstream airflow resulting in partial closure is illustrated in Fig. 3.14 for a fixed upstream pressure. In addition, the longitudinal deformation is illustrated by a simple dye deposit experiment in Fig. 3.15. It is observed that a complete closure can be reproduced as well as an important movement of the deformable portion in the airflow direction during closure.

Deformable symmetrical constriction

A[12] symmetrical deformable constriction is obtained by two connected latex tubes (Piercan Ltd) of 11mm diameter. The tubes are mounted on two metal cylinders with diameter 12mm for which the metal is removed over half the diameter for a length of 40mm. The latex tubes are filled with water supplied through a central duct of 3mm diameter connected to a water column. The same way as for the asymmetrical deformable constriction the height

[10]Main publications: [110].
[11]Main publications: [15, 16, 102].
[12]Main publications: [17, 18, 104].

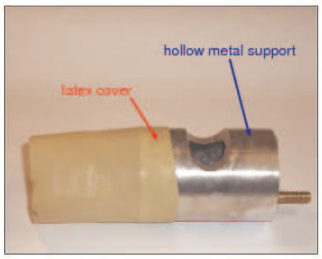

(a) cover and support

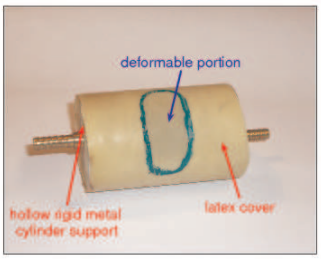

(b) upper cylinder

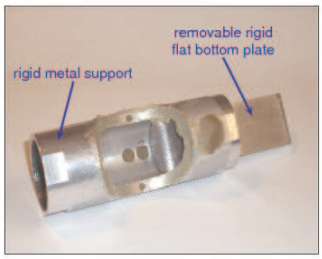

(c) support and flat pate

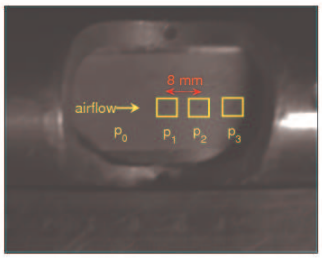

(d) upper view support

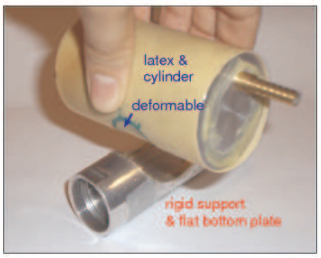

(e) mounting

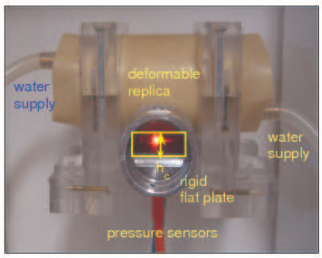

(f) frontal view at downstream end

Figure 3.13: Mounting of the deformable asymmetrical mechanical replica schematised by Fig. 3.12(b): a) latex cover and rigid support, b) resulting deformable upper cylinder, c) rigid support and removable flat bottom plate, d) upper view of rigid support, e) mounting the deformable portion, and f) mounted replica.

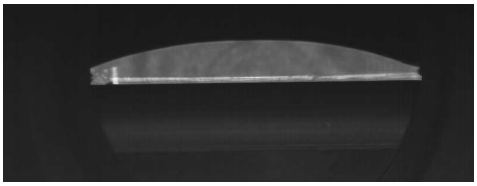

(a) instant 1

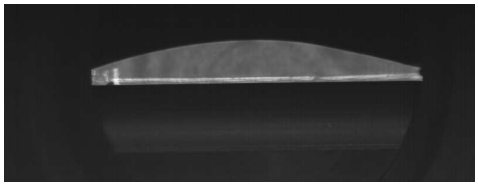

(b) instant 2

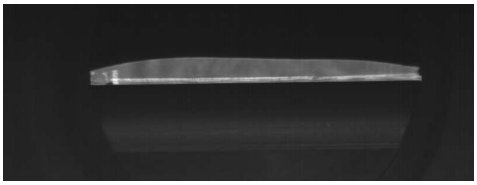

(c) instant 3

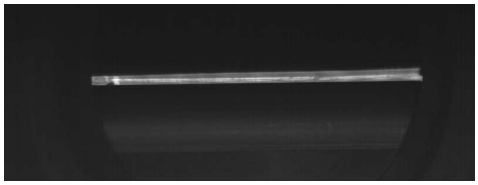

(d) instant 4

Figure 3.14: Illustration of transverse deformation at consecutive time instants.

of the water column, and so internal pressure in the latex tubes, is controllable. The latex tubes are fixated in a metal block in order to prevent leakage. Increasing or decreasing the internal pressure by lifting or lowering the water column implies a change in initial aperture between the two tubes and consequently the two parameters are related in a unique way. In order to vary the initial aperture and the internal pressure in a non-unique way an equal set of uniform rectangular metal shims with fixed length (12mm), fixed width (16mm) and variable thickness can be inserted at the outer borders between the upper and lower portion of the replica separating both latex tube holders to a user controlled extent. This way the initial center aperture at rest is varied from complete closure to a maximum aperture of 10mm. As a consequence the internal pressure and initial aperture are no longer defined

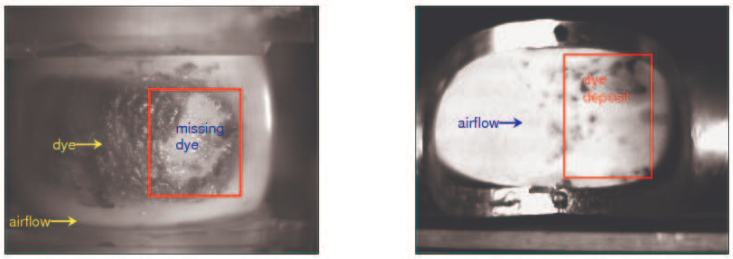

(a) dye suppression on latex cylinder (b) dye deposit on rigid flat plate

Figure 3.15: Illustration of longitudinal deformation from dye deposit of the deformable upper part: a) on the rigid flat plate, b) after a fluid-structure interaction illustrating contact or a total collapse of the deformable tongue replica shown in 3.13 as well as an important movement in the flow direction.

by a 1-1 relationship. Instead different initial apertures are associated with each internal pressure. The deformable symmetrical constriction is illustrated in Fig. 3.16 .

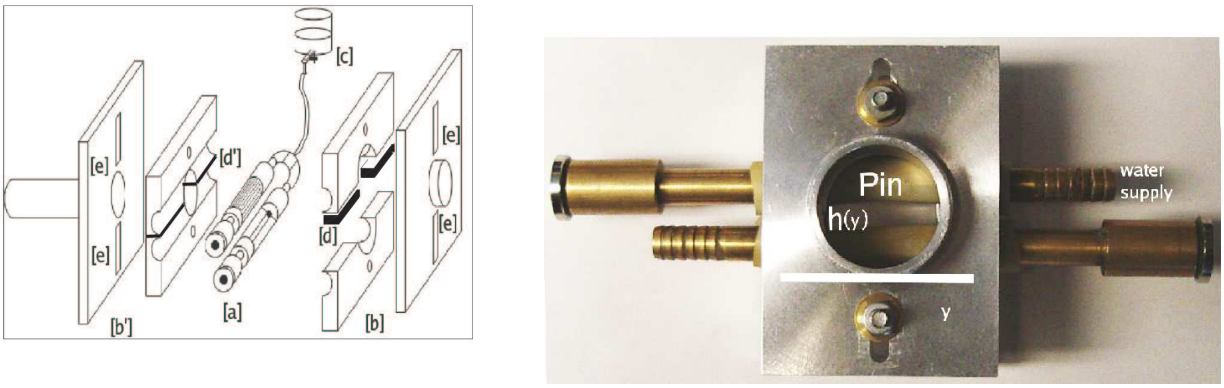

(a) (b)

Figure 3.16: a) Schematic representation of symmetrical deformable replica. Latex tubes [a] are connected to water column [c] enabling to impose the internal pressure P_{in}. Each latex tube is mounted in a metal block [b,b'] by means of fixation screws [e]. The initial geometrical configuration in absence of airflow was characterized by the center aperture h_c^0. h_c^0 is varied 1) by imposing internal pressure P_{in} and 2) by inserting a set of shims [d] between the outer parts of the upper and lower portion of the mounting block. In absence of shims the aperture is minimal [d']. b) Photographic illustration.

The transverse deformation of the deformable symmetrical constriction due to auto-oscillation of the deformable constriction under influece of a given upstream pressure is illustrated in Fig. 3.17(a). The dependence of the deformation on the applied upstream pressure is illustrated in Fig. 3.17(b) and on the internal water pressure in absence of airflow is shown in Fig. 3.17(c).

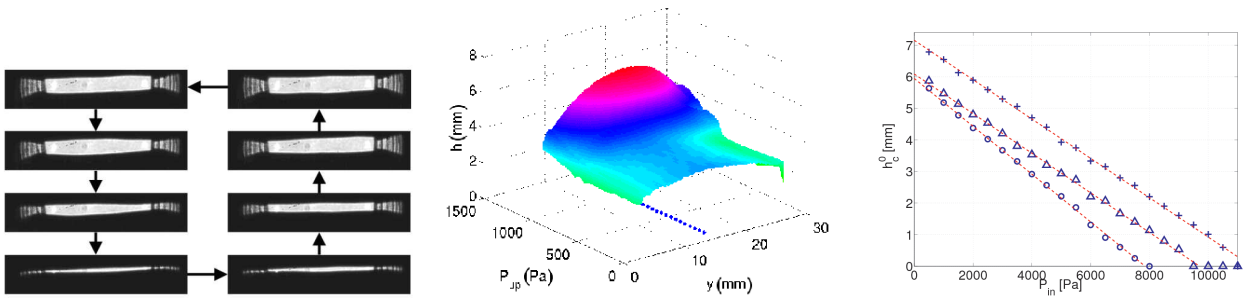

(a) (b) (c)

Figure 3.17: Illustration of deformation: a) consecutive time instants, b) Exemplary aperture feature extraction $h(y, P_{up}, P_{in})$ as function of upstream pressure P_{up} ranging from 0 up to 1500 Pa. The dotted line indicates the centre line $y = 15$mm, c) measured initial center apertures $h_c^0(P_{in}, d)$ for shims $d = 1.0$ (+), $d = 0.5$ ($\triangle$) and $d = 0.0$ ($\circ$) mm as function of P_{in}. The dashed lines indicated a linear fit for each shim set with slope -0.00062, -0.00063 and -0.00076 for shims 1.0, 0.5 and 0.0 respectively.

Chapter 4

Characterisation of jet development

Some examples of qualitative and quantitative characterisation of jet development at the exit of some of the nozzles described in the previous chapter are summarised in the following.

4.1 Round free jet development

Despite the reported universal behaviour for an axisymmetric jet, the influence of initial conditions and geometry on axisymmetrical jet development is put forward from analytical arguments, numerical simulations as well as experimental evidence. In among others [31, 32] it is shown analytically that the averaged equations of motion for a number of flows admit to more general similarity solutions that retain a dependence on both the Reynolds number and the initial conditions. Consequently, decay rate constant K and the virtual origin depend on conditions at the tube outlet. Those analytical findings were in agreement with earlier experimental results of [41, 59, 71, 113] illustrating among others the influence of initial conditions on the development of coherent structures and consequently on the spreading rate for Reynolds numbers $Re > 10^4$. More recent experimental studies confirmed these earlier findings by putting into evidence the influence of initial conditions as well as nozzle geometry features: e.g. nozzle diameter [63], nozzle shape [67, 76], boundary layer thickness [47, 82], exit velocity profile [6, 115], exit grid [13] and Reynolds number [75, 78]. In addition, the influence of the initial velocity profile at the tube exit is shown by means of numerical simulations [11].

Most of the cited studies deal with Reynolds numbers $\geq 10^4$. Nevertheless, in particular jets associated with moderate Reynolds numbers, $Re < 10^4$, appear to be sensitive to initial conditions [32, 63]. Experimental studies dealing with the influence of diameter d and inital mean velocity U_0 on the centerline velocity decay of axisymmetric jets with uniform initial outlet profile at moderate Reynolds numbers are presented in [63, 71]. Those studies show that the centerline velocity decay coefficient decreases and the half-width spread angle increases for decreasing outlet Reynolds numbers. Moreover in [63] it is concluded that the velocity decay coefficients are best correlated by the nozzle centerline velocity at the outlet U_0. Both studies [63, 71] dealt with ASME Standard Long Radius Nozzles with diameters 0.1524, 0.0758 and 0.0401m for Reynolds numbers of order $Re \approx 10^4$ and turbulence intensities below 9%. Obviously, data for moderate Reynolds numbers, $Re < 10^4$ and non-standard nozzle geometries are less studied.

4.1.1 Extended convergent-divergent nozzle

The[1] spatial jet development is sought for given initial momentum $M_0 = \pi d^2 U_b^2/4$, i.e. constant tube diameter $d = 25mm$ and constant initial bulk velocity $U_b = 4.4m/s$ resulting in moderate Reynolds $Re = 7350$ and low Mach number flow of order 10^{-2}. The influence of extension tube length L_t on the velocity profile at the tube outlet and on the resulting jet development is sought. Jet development is measured by scanning the velocity field with hot-film single sensor anemometry from the tube exit up to 20 times extension tube diameter d.

The following observations are made:

I) Both the shape of mean (Blasius to top-hat) and fluctuating portion (rms 6-50%) of the initial velocity profile at the tube outlet are severly altered as the ratio L_t/d decreases reflecting the influence of the upstream diffuser on initial conditions. Consequently, for the range of flow and geometrical conditions studied, varying the extension length downstream a convergent-divergent diffuser is a natural way to vary initial conditions. Initial conditions are illustrated in Fig. 4.1.

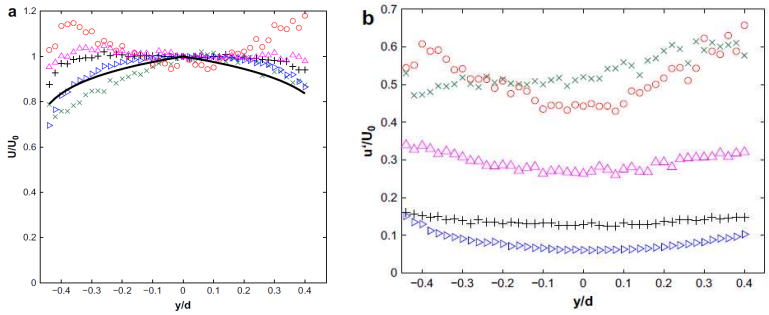

(a) U/U_0 (b) u'/U_0

Figure 4.1: Initial conditions at tube exit ($x/d < 0.01$) for L_t/d 0.4 ($\times$), 1.2 ($\circ$), 3.6 ($\triangle$), 7.2 ($+$) and 20 ($\triangleright$): a) normalised mean velocity U/U_0 and Blasius profile (full line) b) normalised rms of velocity u'/U_0.

II) With respect to centerline and transverse mean velocity modelling it is shown that self-similar models can be applied regardless the initial conditions. Nevertheless, established relationships between common model parameters such as the centerline velocity decay $K \sim U_0$ and the spreading rate $S \sim 1/U_0$ are inversed as the initial turbulence level increases from 12 up to 27%. Additional data in this turbulence range should be considered to establish a region for which the relationship $K \sim U_0$ is inversed due to high initial turbulence levels which favours velocity decay. Moreover, additional data might allow the relationship of the centerline velocity decay with U_0 to be extended to account for the initial turbulence level. With respect to upper airway geometries and flow conditions, self-similar jet models can be applied although parameters need to be adapted depending on the initial turbulence level and initial mean velocity U_0. Application of self-similar jet models is illustrated in Fig. 4.2.

III) Comparing transverse and centerline turbulence statistics, i.e. rms and skewness, for all assessed extension tubes illustrates the difference in shear layer development. Centerline turbulence statistics yield asymptotic values for $x/d \geq 8$ for which the value depends on the initial turbulence level and so on L_t/d. The difference in shear layer development is also observed in the one-dimensional velocity spectrum. The spectra exhibit a common inertial

[1] Main publications: [35, 107].

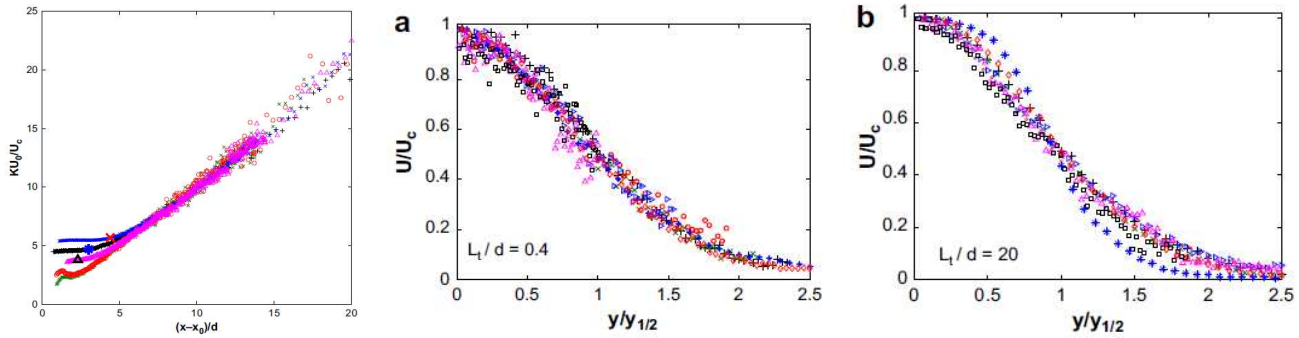

(a) centerline (b) transverse $L_t/d = 0.4$ (c) transverse $L_t/d = 20$

Figure 4.2: a) Inverse normalised longitudinal mean centerline velocities compensated for the self-similar law KU_0/U_c : L_t/d 0.4 ($\times$), 1.2 ($\circ$), 3.6 ($\triangle$), 7.2 ($+$) and 20 ($\triangleright$). The potential core x_p in the self-similar representation is indicated for L_t/d 3.6 ($\triangle$), 7.2 ($*$) and 20 ($\triangleright$) and b,c) Similarity representation of transverse normalised axial mean velocity profiles U/U_c for x/d 1.6 ($\star$), 3.2 ($\diamond$), 4 ($+$), 4.8 ($\times$), 6.4 ($\circ$), 8 ($\triangleright$), 12 ($\triangle$), 16 ($\square$).

range of limited extent due to the moderate Reynolds number followed by a decay range which depends on L_t/d in accordance with the difference in turbulence development. Shear layer development and spectra are illustrated in Fig. 4.3.

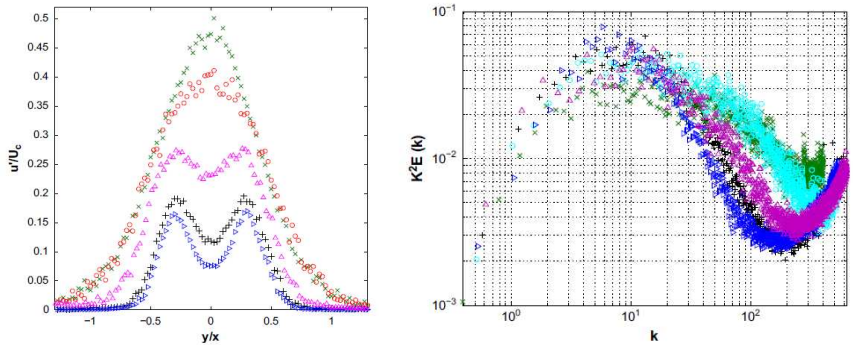

(a) (b)

Figure 4.3: a) Normalised transverse rms velocity at $x/d = 1.6$ for L_t/d 0.4 ($\times$), 1.2 ($\circ$), 3.6 ($\triangle$), 7.2 ($+$) and 20 ($\triangleright$) and b) One dimensional velocity spectra at $x = 1.6d$ at maximum shear stress position for L_t/d 0.4 ($\times$), 1.2 ($\circ$), 3.6 ($\triangle$), 7.2 ($+$) and 20 ($\triangleright$) where $k = \omega d/U_c(x)$ denotes the dimensionless wavenumber.

IV) Since a gradient-transport model is generally assumed to hold near the centerline of an axisymmetrical jet, turbulent viscosity near the centerline is estimated in order to assess the shear stresses in this region as well as to obtain a qualitative estimation away from the centerline. Two-component velocity measurements are required to obtain an accurate measurement of the shear stresses in order to validate the shear stress estimations over a large range of initial turbulence intensities. Nevertheless, the current turbulent viscosity and shear stress estimations provide a qualitative estimation which might be applied in modelling. Relevant quantities are illustrated in Fig. 4.4.

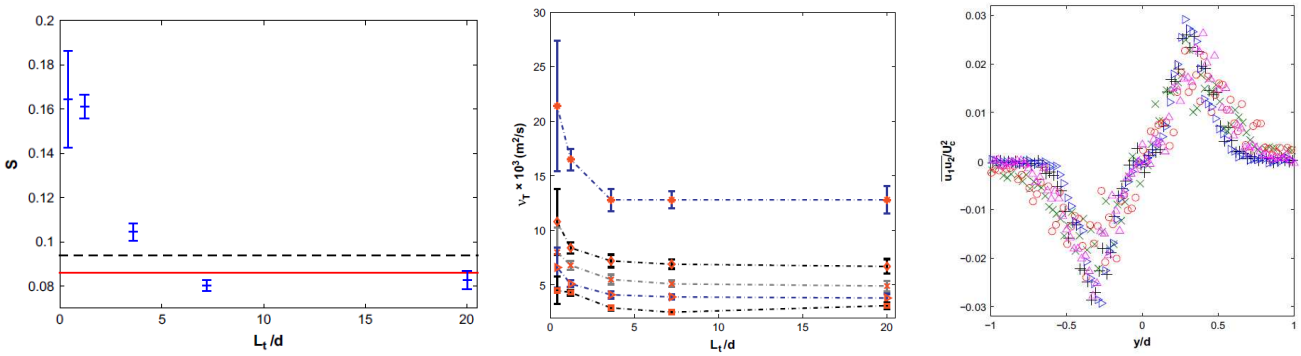

(a) (b) (c)

Figure 4.4: a) Spreading rates $S(L_t/d)$, 0.094 (dotted) and 0.086 (full) are derived from [48] and Gaussian function with $n = 94$, b) Experimental turbulence viscosity $\nu_T(L_t/d)$ at x/d 1.6 ($\star$), 3.2 ($\diamond$), 4.8 ($\times$), 8.0 ($\triangleright$) and 16 ($\square$) and c) Normalised estimated shear stresses at $x/d = 1.6$ for L_t/d 0.4 ($\times$), 1.2 ($\circ$), 3.6 ($\triangle$), 7.2 ($+$) and 20 ($\triangleright$).

4.1.2 Extended sharp contraction nozzle

The[2] motivation to study jet flow at the exit of an extended sharp contraction nozzle follows the motivation given earlier for the extended convergent-divergent nozzle. Former investigations are essentially conducted for industrial purposes and reported results are obtained for high bulk Reynolds number flow, typically 10^4 or higher, and for geometrical configurations either aiming optimal nozzle design or developed pipe flow for which the length-to-diameter ratio exceeds 40 with well controlled flow entrance to the nozzle. Although studies at low Reynolds number have been conducted [2, 3, 53] few information is available of the influence of the tube extension length downstream an sharp constraction. Varying the extension length is a simple flow control device. Consequently, increased understanding of the flow behaviour is required to describe flow development and vortex generation in the mixing layer of the round jet.

So the effect of a sharp contraction coupled with a downstream circular tube with varying length-to-diameter ratio is sought for different moderate bulk Reynolds numbers $1000 < Re_b < 1.2\times10^4$. Hot-film anemometry measurements and smoke visualisation are reported here in order to evaluate the effects of two length-to-diameter ratios $L/D \in \{1.2, 53.2\}$, coupled with sharp angles, over 19 Reynolds numbers ranging from 1131 to 11320. The experimetal setup and smoke visualisation are illustrated in Fig. 4.5. Main results shown deal with the mean velocity exit profile, the turbulence intensity, the centerline velocity decay rates, the virtual origin in the near field of the jet ($x/D < 20$) and the generation of coherent structures.

The following observations are made:

Despite significant differences between the assessed length-to-diameter ratios, similarities in the overall jet behaviour are found:

- For Reynolds number $Re_b > 4527$, the potential core x_{pc} is found to increase with Reynolds number. Although this evolution is in opposition with some previous studies on smooth contraction nozzle shapes, a good overall agreement with the models developed by [42,86] generally applied/valid for higher Reynolds numbers,

[2]Main publications: [35,36].

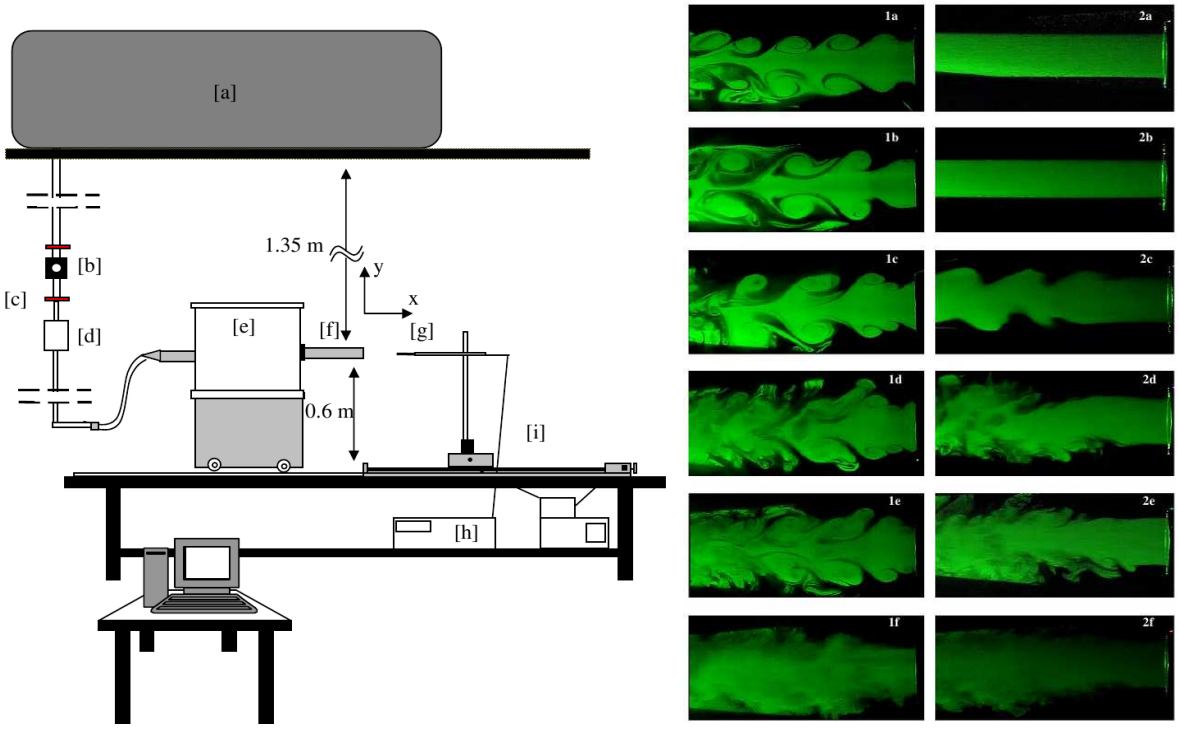

Figure 4.5: a) Schematic view of the setup during anemometry [a] air compressor, [b] pressure regulator, [c] valve, [d] volume flow rate, [e] settling chamber, [f] pipe section, [g] hot film, [h] IFA-300 TSI, [i] positioning system carrying the hot film. b) Instantaneous images of jet flows for the two assessed length-to-diameter ratios $L/D = 1.2$ (1) and $L/D = 53.2$ (2) for Reynolds numbers Re_b 1132 (1-2a), 1697 (1-2b), 2263 (1-2c), 2824 (1-2d), 3961 (1-2e), 11317 (1-2f).

is observed as shown in Fig. 4.6(a).

- The velocity decay constant K increases with Reynolds number Re_b due to a reduced flow mixing with the surrounding flow illustrated in Fig. 4.6(b).

- As Reynolds number Re_b is increased, the virtual origins x_0 of the jet flow moves continuously upstream leading to the observation of negative values analysed as the consequence of back flow.

- The initial centerline turbulence intensity is decomposed into two regimes in function of the Reynolds number Re_b as shown in Fig. 4.6(c). In the range $1132 < Re_b < 2200$ the initial centerline turbulence intensity increases with Reynolds numbers before continuously decreasing for higher Reynolds numbers towards an asymptotic value as observed in literature.

Nevertheless, the applied length-to-diameter ratio L/D downstream the coupled sharp edged tube inlet is seen to affect:

- The initial mean velocity profiles at the tube exit, illustrated in Fig. 4.7(a), shift from a Poiseuille profile to a 1/7 power law velocity profile as the Reynolds Re_b number is increased for $L/D = 53.2$. The observed

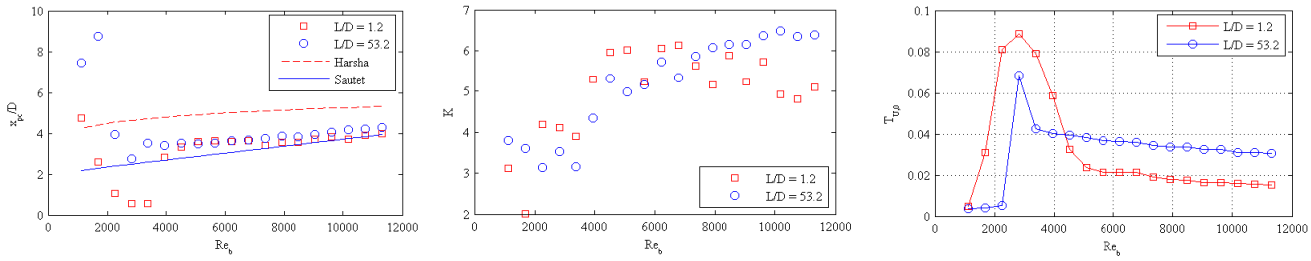

(a) (b) (c)

Figure 4.6: For $L/D = 1.2$ and $L/D = 53.2$: a) Normalised potential core extent x_{pc}/D as function of Reynolds number Re_b. b) Normalised velocity decay constant K as function of Reynolds number Re_b. c) Initial centerline turbulence intensity profiles $T_{U,0}(y/D = 0, x/D = 0)(Re_b, L/D)$ as function of Reynolds number Re_b.

shift is in accordance with previous studies. For the smallest ratio $L/D = 1.2$ a trapezoidal velocity profile is generated at the tube exit for all assessed Reynolds numbers Re_b .

- The initial transverse turbulence intensity profile at the tube exit, illustrated in Fig. 4.7(b), shows a complex variation for $L/D = 1.2$. In the wall vicinity a region of turbulence dissipation is observed at low Reynolds numbers Re_b.

- For $L/D = 1.2$, the longitudinal mean jet centerline velocity in the near field, $0 < x/D < 5$, exhibits a singular behaviour with a velocity evolution decomposed into 2 phases: a strong velocity decrease followed by a constant velocity portion shown in Fig. 4.8(a). In parallel, the turbulence intensity T_u presents a peak intensity in the range $1620 \leq Re_b \leq 4527$ illustrated in Fig. 4.8(b). The observation of such phenomena is similar to [99], where the jet issues from a smooth convergent nozzle. Smoke visualisation illustrates the the formation of toroidal ring vortices in this range of Reynolds numbers shown in Fig. 4.5(b). As the Reynolds number Re_b is increased we observe the formation of a secondary vortex in the tail of the first one due to the upstream presence of sharp edges, and a pairing phenomenon. This observation is confirmed by the observed velocity power spectra for which a large and a thin peak is found. Some spectra are illustrated if Fig. 4.9. In case of $L/D = 53.2$, the mean centerline velocity decreases slowly and continuously, with no hump in the turbulence intensity.

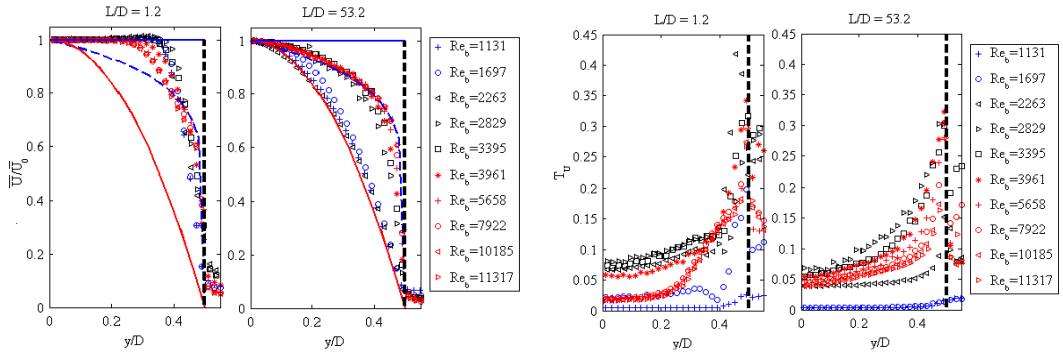

(a) (b)

Figure 4.7: For $L/D = 1.2$ and $L/D = 53.2$: a) Mean velocity profiles and b) Turbulence intensity profiles.

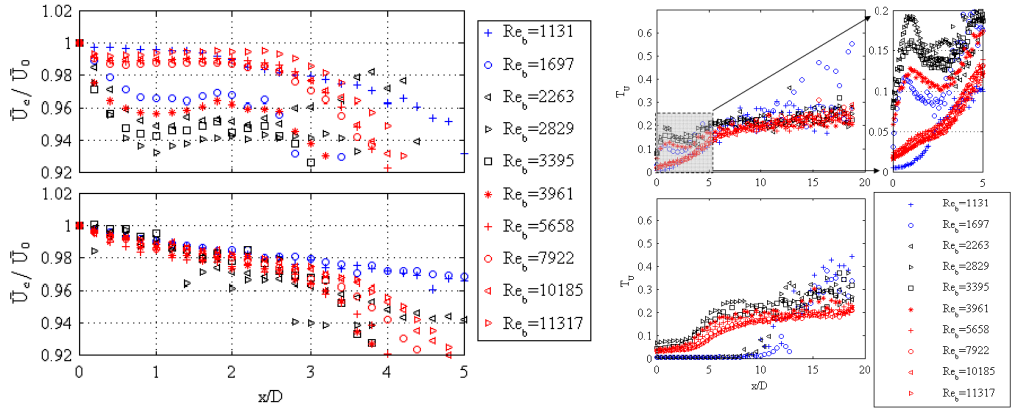

(a) (b)

Figure 4.8: For $L/D = 1.2$ (upper) and $L/D = 53.2$ (bottom): a) Normalised mean centerline mean velocity in the near field downstream region $0 < x/D < 5$. b) Centerline turbulence intensity T_U.

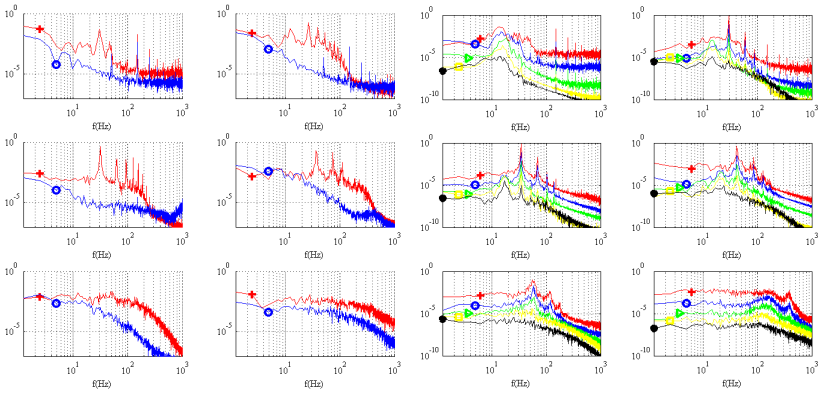

(a) (b)

Figure 4.9: For Reynolds numbers $Re_b = \{1132, 1697, 2263, 2824, 3961, 11317\}$: a) Power spectra at the position $(x/D = 0, y/D = 0.5)$. The spectra for $L/D = 53.2$ are shifted one decade downwards with respect to $L/D = 1.2$. b) Power spectra of centerline of velocity signals for $L/D = 1.2$ at five downstream positions $x/D = \{1(\times), 2(\square), 3(>), 4(\circ), 5(+)\}$. Every spectrum is shifted one decade downwards with respect to the previous.

4.1.3 Mean jet decay model parameters

The[3] time averaged turbulent jet flow mixing region is schematically divided into three parts: an initial near field region downstream the exit, a transition region and a self-preserving far field region further downstream. In this third zone, the axisymmetrical jet flow is typically modelled by a simple decay equation [87].

$$\overline{U}_c(x) = \frac{\overline{U}_0 K D}{x - x_0}, \tag{4.1}$$

with $\overline{U}_c$ denoting the mean centerline velocity, $\overline{U}_0$ the centerline mean velocity at the exit, K the mean centerline velocity decay coeffiecient and x_0 the virtual origin as illustrated in Fig. 4.10. The decay model is illustrated for the convergent-divergent nozzle in Fig. 4.2(b) where the mean centerline velocy compensated for the self-similar decay model is plotted. The influence of inlet geometry, tube extension L/D and Reynolds number Re_b on the flow

[3] Main publications: [35, 36, 38].

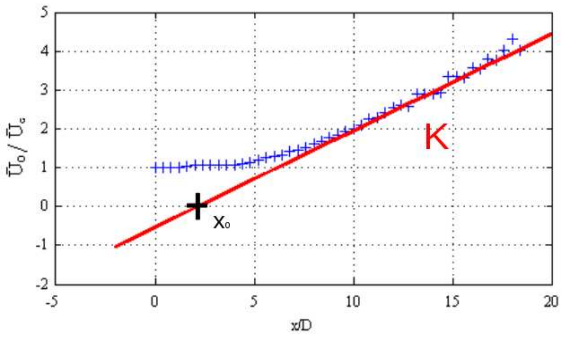

Figure 4.10: Illustration of the self-similar jet decay model and its parameters: decay constant K and virtual origin x_0.

development and therefore on the model coefficients is shown in the previous section and findings are summarised in Table 4.1 for an abrupt reduction. In case the tube extension is preceeded by a diffuser the influence of the tube extension length L/D is enforced compared to an abrupt reduction and the observed turbulence intensity T_U and decay constant K are seen to depend mainly on the tube extension length L/D [35].

Table 4.1: Overview of influence of Reynolds number Re_b and extension length L/D on jet development: intial velocity profile, turbulence intensity T_U, vortex strucutes, model coefficients (K, x_0).

	Sharp extended nozzle	
	Re_b	L/D
Singular initial velocity profiles (reducion of boundary layer)		L/D
Turbulence intensity $T_{U,0}$ Turbulence intensity peak T_U	Re_b $1131 < Re_b < 4000$	L/D
Vortex structures	Re_b	L/D
Model coefficients (K, x_0)	Re_b	

In Table 4.2 values of the model coefficients (K, x_0) reported in literature are compared to values from the sharp extended nozzle for $Re_b = 11318$ illustrating that for the largest experimentally assessed Re_b the decay constant K is within the range reported in literature.

4.2 Rectangular free jet development

4.2.1 Rectangular nozzle with 1 sharp obstacle

Flow[4] through asymmetrical nozzle geometries occurs naturally in different aspects of daily life. Despite their relevance most research efforts deal with well designed symmetrical nozzles under impulse of aeronautic applications [8, 46, 69]. Moreover, the same way as for axisymmetrical nozzles, most research on plane, wall or slot jet studies deals with large Reynolds numbers ($Re_b \gg 5000$), e.g. tabled overviews reported in [40, 41, 55, 88], data for low to moderate Reynolds number flows are few. A recent study concerning the influence of Reynolds number ($1500 < Re_b < 16500$) on orifice plane jet development points out that the effect on the mean and turbulent field is

[4]Main publications: [106].

Table 4.2: Overview of reported model constants depending on geometry (convergent or tube L/D), Reynolds number Re_b and exit centerline turbulence intensity $T_{U,0}$.

		Re_b	x_0/D	K	$T_{U,0}$	L/D
Literature	Wygnanski & Fiedler [114]	10^5	3	5.7		convergent
	Panchapakesan & Lumley [73]	1.1×10^4	-2.5	6.06		convergent
	Hussein *et al.* [48]	9.5×10^4	4	5.8		convergent
	Mi *et al.* [68]					
	- convergent	1.6×10^4	3.5	4.45	0.5%	convergent
	- long tube	1.6×10^4	4.73	4.63	3%	72
	Mi *et al.* [67]	72000			3%	39
	Fellouah *et al.* [27]	$6 \times 10^3 - 3 \times 10^4$	5.59	2.5	3%	convergent
	Xu & Antonia [115]					
	- convergent	8.6×10^4	3.7	5.6	0.5%	convergent
	- long tube	8.6×10^4	2.6	6.5	4%	118
Sharp	Grandchamp *et al.*					
	- short tube	11318	0.7	5.1	1.6%	1.2
	- long tube	11318	-0.35	6.38	4%	53.2

particularly substantial for $Re_b < 10000$ [21].

The dependence of near-field flow structures of an orifice jet on the upstream nozzle profile for $Re_b > 5000$ [45, 66] confirms the influence of initial conditions on jet dynamics and near field shear layer development and entrainment [32, 40, 43, 85]. Nevertheless, the influence of Reynolds number on jet development is still unclear and contradictory experimental results are reported for important mean flow features such as the decay rate in the near field region [21, 40, 66]. So that flow characterisation in the near field is necessary. Experimental visualisations of coherent structures are used to study flow structures [99, 112] and to obtain a quantification of temporal and spatial vortex features such as reported for the first downstream vortex for a pulsed round jet [49]. Temporal vortex shedding and the spatial growth rate are of great interest for use with a theoretical description of how this vortex motion produces sound [10, 44, 52].

The current study contributes to the study of low to moderate Reynolds numbers ($100 < Re_b < 1100$) plane jet development for an original asymmetrical nozzle. The asymmetrical rectangular nozzle is obtained by inserting a sharp-edged trapezoidal obstacle in a rectangular channel upstream the nozzle exit at 1.47 times the minimum aperture h depicted in Fig. 3.9. Resulting initial velocity profiles at the obstacle trailing edge are asymmetric due to the asymmetric upstream flow acceleration, whereas immediately downstream the obstacle trailing edge the flow is basically thought of as a two-layer shear flow consisting of an inner layer (boundary layer) and an outer layer (similar to a free shear layer) [23, 33, 87]. It is sought to experimentally quantify main spatial and temporal features of the resulting near field jet vortex dynamics by smoke visualisation [45, 49, 93, 116] realised with the setup depicted in Fig. 4.11(a). Image features are extracted from smoke visualisations in order to study the overall temporal and spatial behaviour of vortex structures in the near field downstream the asymmetrical nozzle.

Vortex dynamics in the near field downstream an asymmetrical rectangular nozzle for low to moderate bulk Reynolds numbers ($100 < Re_b < 1100$) are studied based on rectangular vortex features — *i.e.* width, height and center position illustrated in Fig. 4.11(b) — extracted from smoke visualisation images. The influence of the bulk Reynolds number Re_b on the spatial and temporal evolution of counterclockwise and clockwise vortices is assessed and the

influence of the asymmetry is outlined.

The following observations are made:

I) Spatial characterisation of mean streamwise and transverse center positions of 1 up to 3 counterclockwise and clockwise vortices shows 1) an asymmetry of the spatial distribution of the mean center coordinates between counterclockwise and clockwise vortices and 2) a reduction of the spatial life-span of the vortices from $x/h < 15$ to $x/h < 5$ as Re_b increases in the range $100 < Re_b < 1100$. The observed asymmetry is most pronounced for the first vortices situated immediately downstream the nozzle exit stressing the influence of the asymmetry of the nozzle on the flow development. This finding encourages further studies of the influence of the aperture as well as the obstacle placement with respect to the nozzle exit on the spatial jet vortex dynamics and associated transition to turbulence.

II) The width-to-height ratio $R < 1$ for the first counterclockwise as well as first clockwise vortex indicates that vortices immediately downstream the nozzle exit are stretched in the transverse direction independently of Reynolds number Re_b. As the vortices are convected downstream R increases, *i.e.* vortices are stretched in the streamwise direction, with a rate depending on the Reynolds number illustrated in Fig. 4.12.

III) The vortex shedding rate f_v is found to increase linearly with bulk Reynolds number Re_b. From this relationship the Strouhal number is seen to increase with Reynolds number Re_b and an analytical approximation for $St(Re_b)$ is proposed depending on the linear regression parameters (α, β) describing $f_v \propto Re_b$ and minimum aperture h. The findings are illustrated in Fig. 4.13.

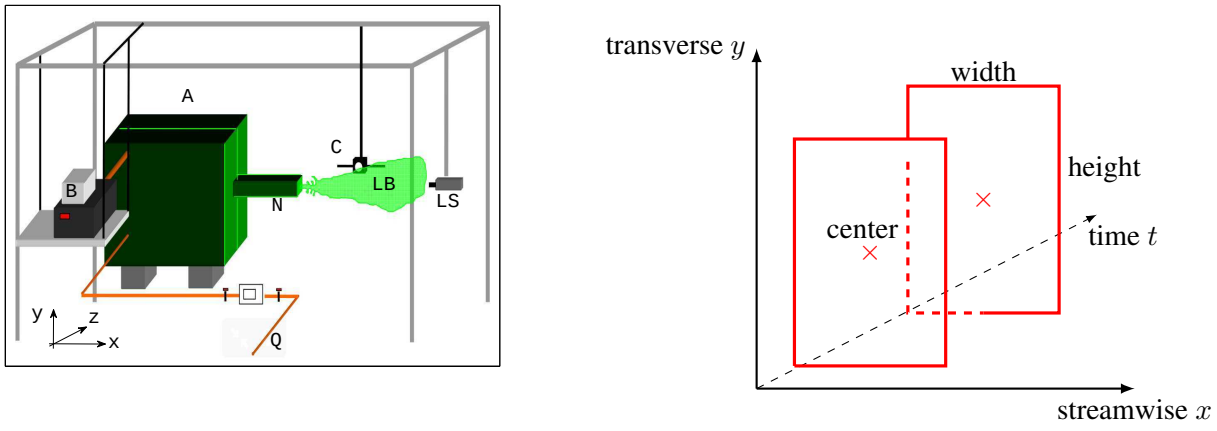

(a) (b)

Figure 4.11: a) Schematic representation of the experimental setup for smoke visualisation: 1) settling chamber (A) of volume 0.112m^3 with dimensions $56 \times 50 \times 40$cm to which the nozzle (N) represented in Fig. 3.9 is attached, 2) smoke generation and injection (B), 3) volume airflow rate supply (Q) with pressure regulator and thermal mass flow meter, 4) laser source (LS) with cylindrical lens ($\theta_3 = 10°$), 5) high speed camera (C) perpendicular to the laser sheet (LB). The laser source (LS) and camera (C) are mounted on a three-dimensional rail system. The x-axis indicates the main flow direction. b) Schematic representation of sought spatial vortex features derived from an enveloping rectangle (center position, height and width) and their time evolution.

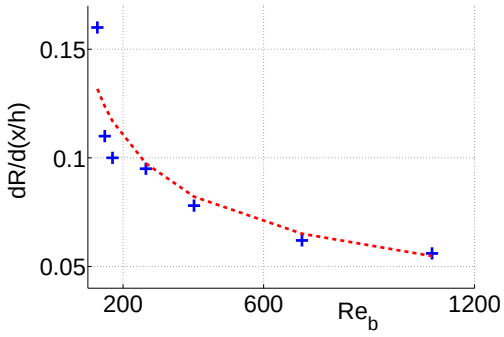

Figure 4.12: The growth speed of width-to-height ratio R in the streamwise direction x/h as a function of Reynolds number, $\frac{dR}{d(x/h)}\,(Re_b)$, and the functional approximation $\approx 0.96 \times Re_b^{-0.41}$ (dashed curve).

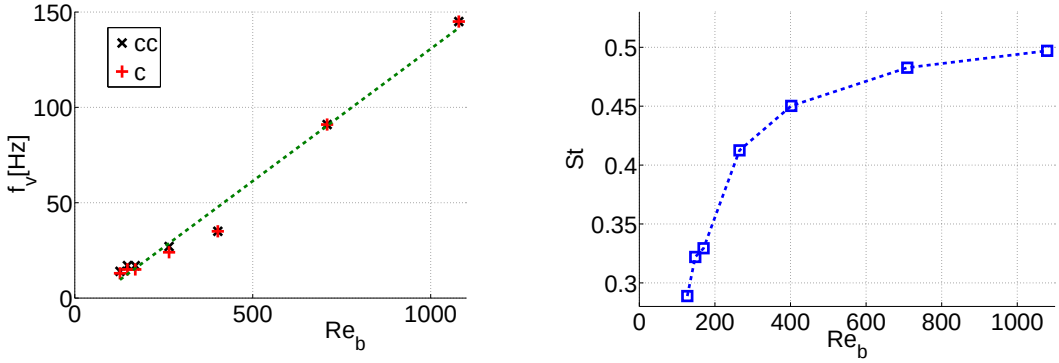

(a) $f_v(Re_b)$ (b) $St(Re_b)$

Figure 4.13: Estimation of a) vortex shedding frequency $f_v(Re_b)$ [Hz] and approximation as $f_v(Re_b) \approx 0.14 \times Re_b - 8$ and b) Strouhal number $St(Re_b)$ resulting from f_v-values for counterclockwise (cc) and clockwise (c) vortices as well as for the linear approximation $f_v(Re_b, h) \approx 0.14 \times Re_b - 8$ (linear). The relationship can be described as $St(Re_b) \approx \left[\alpha + \frac{\beta}{Re_b}\right] \frac{h^2}{\nu}$ with ν the kinematic viscosity, $\alpha = 0.14$ and $\beta = -8$.

IV) Based on current experimental findings it is suggested that vortex shedding is associated with the shear-layer mode of Kelvin-Helmholtz vortices.

V) Estimated Strouhal numbers $0.28 < St(Re_b) < 0.5$ are larger than values reported for plane orifice jets [32, 43, 45, 85] indicating the influence of the asymmetric geometry on the flow development and its transition to turbulence. Retrieved values approache the upper limit of values retrieved for plane jets $0.3 < St < 0.64$ at much higher Reynolds numbers $Re_b > 10000$ [41].

Chapter 5

Validation of flow models

Some examples of validation of flow models are given.

5.1 Convergent axisymmetrical nozzle

Studies[1] dealing with wind tunnel design are multiple illustrating the importance of the upstream geometry on the flow characteristics at the inlet of a wind tunnel working section [8, 25, 51, 65, 69]. Besides, characterisation of the exit profile of the nozzle, corresponding to the inlet portion to the working section, attention is given to avoid adverse pressure gradients along the nozzle walls in order to favour low turbulence inflow to the working section.

Despite the amount of research available in aeronautics, inflow conditions are not or only marginally accounted for when designing an experimental flow facility for experimental validation on a smaller scale. Nevertheless, a laminar inflow with known boundary layer characteristics is of interest in order to limit the influence of upstream flow conditions on downstream flow development and noise production.

Obviously, the sought laminar and known inflow conditions can be obtained by mounting a pipe upstream the replica in order to ensure a fully developed Poiseuille flow. Nevertheless, for the aimed range of moderate Reynolds numbers the required pipe length results in a large experimental setup (orders of meters [50, 56, 117]) so that a smaller setup is if not more practical at least more elegant. Consequently, it is chosen to study a short contraction geometry of limited length (6cm) depicted in Fig. 3.6 and fully described by (3.3) with a geometrical scale adapted to applications favouring a small-sized nozzle.

In order to test the contraction experimentally, accurate transverse velocity profiles at the exit of the proposed axisymmetrical contraction nozzle with contraction ratio $CR = 21.8$ and lenght 6cm are measured by hot-film anemometry from which boundary layer characteristics can be derived [12, 87, 111]. As such the experimentally estimated boundary layer characteristics provide data in order to validate laminar flow models since the turbulence level at the nozzle centerline exit is less than 1% for all velocities.

[1] Main publications: [30, 39].

The flow through the nozzle is modelled with Thwaites axisymmetrical boundary layer solution [79, 97, 98] in order to validate the dependence of the shape factor and skin friction parameter on the Thwaites parameter instead of relying on tabulated values reported in literature [9], since it is known that the dependence on Thwaites parameter varies with the flow and geometrical conditions. Consequently, the sought experimental validation of Thwaites method is two-fold in order to validate the measured flow characteristics at the nozzle exit as well as to consider the influence of the dependence of the shape factor and skin friction parameter on Thwaites parameter for low to moderate Reynolds numbers in the range $300 < Re < 20200$.

The following observations are made:

I) It is observed on the measured exit velocity profiles that the variation in the mean velocity is lower than $\pm 0.5\%$ for all assessed Re whereas the boundary layer grows rapidly for $Re \leq 3300$. In addition, velocity measurements in the boundary layer with high spatial accuracy (spatial step of $10\mu m$) are performed to estimate the displacement thickness δ_1, momentum thickenss δ_2 and shape factor H. Consequently, the proposed nozzle is of use for applications requiring low turbulence inflow and known boundary layer characteristics at the exit of a nozzle with limited size as is the case for experimental validation of flow modelling.

II) Thwaites laminar axisymmetrical boundary layer solution using modified universal functions is applied to model the flow through the nozzle. Two constants are introduced in the universal functions describing the skin friction parameter and the shape parameter in order to account for the influence of flow and geometrical conditions. Comparing modelled and measured quantities at the nozzle exit shows that Thwaites solution provides good predictions for $Re > 3300$, *i.e.* before the onset of boundary layer growth as shown in Fig. 5.1(a). Furthermore, in general it is seen that in particular when boundary layer characteristics are of interest adding non-zero constants (denoted $c_{H,S} \neq 0$) to the universal functions increases the model accuracy in particular as the Re-number decreases.

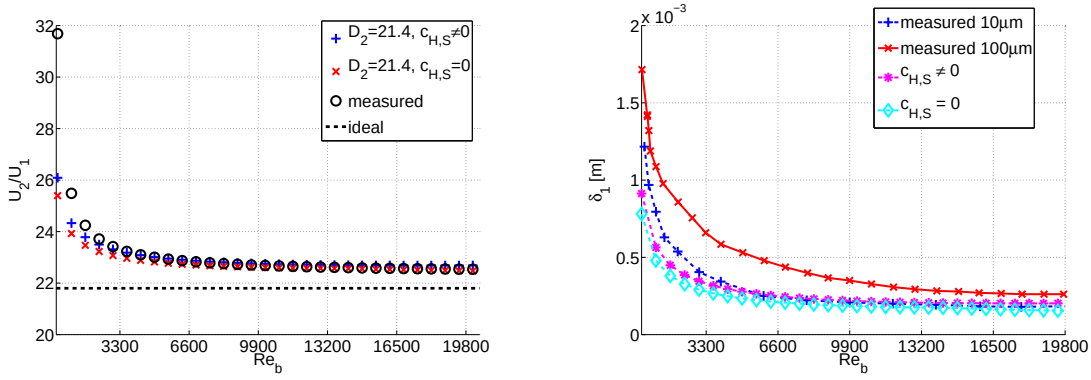

(a) (b)

Figure 5.1: a) Measured and modelled exit centerline velocity U_2 normalised by the inlet centerline velocity of the nozzle U_1 for a fixed contraction ratio of $CR = 21.8$ (dashed line) associated with an ideal fluid in a contraction. As a reference also the measured centerline velocity is indicated. Modelled values are obtained for the additional coefficients set to zero ($c_{H,S} = 0$) or not ($c_{H,S} \neq 0$). b) Comparison of modelled and measured displacement thickness δ_1 at the exit of the nozzle with $CR = 21.8$. As before additional coefficients are set to zero ($c_{H,S} = 0$) or not ($c_{H,S} \neq 0$).

5.2 Asymmetrical constriction

The[2] pressure distribution along an rigid asymmetrical channel constriction depicted in Fig. 3.12 is predicted from the upstream pressure and geometrical information. Several assumptions on the flow and the constriction geometry are experimentally assessed. The model performance of corresponding flow models with increasing complexity is systematically and quantitatively validated.

The following observations are made:

I) It is shown from a dimensionless analysis that, in first approximation, the fluid flow through the 'in-vitro' replica can be described as steady and incompressible. Measured velocity profiles and measured pressures at different places along the converging part of the constriction confirmed the relevance of a bidimensionnal flow description whereas the viscous pressure losses can be neglected outside the boundary layer. Furthermore the velocity profiles reveal an asymmetry of the flow downstream of the constriction due to the geometrical asymmetry illustrated in Fig. 5.2.

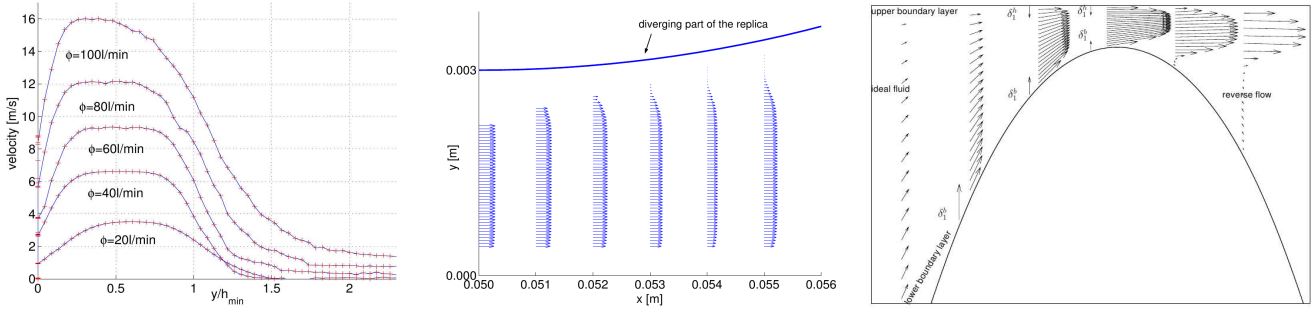

(a) (b) (c)

Figure 5.2: a) Measured vertical (y-axis) velocity profile at 9mm downstream the minimum constriction of 2.3mm. Note the asymmetrical flow behaviour for $\phi = 100$l/min. b) Measured bidimensional velocity profile illustrating jet formation and flow separation along diverging part of replica for steady flow of $\phi = 40$l/min and minimum aperture 3mm. A step of 1mm is applied in the longitudinal x-direction and 0.05mm in the transverse y-direction. c) Reduced Navier Stokes (RNSP) computation ($Re_b = 500$). The two uppper and lower boundary layers and the ideal fluid appear from the computation. The interaction between the ideal fluid and the boundary layers is the core of the Interactive Boundary Layer theory [54].

II) Transversal pressure measurements on both sides of the constriction show that the influence of the asymmetry on the measured pressure within the constriction is negligible. This point is further confirmed by considering the predictions obtained by a two dimensional flow description from the boundary layer solution and Reduced Navier Stokes simulations. The use of these two dimenstional flow descriptions result in a physical prediction of the position of flow separation as illustrated in Fig. 5.3.

III) It is found that the outcome of a classical one dimensional flow description is sufficient in applications where only prediction of the volume flow is strived, but fails to predict the pressure distribution as shown in Fig. 5.4. Quantitative experimental validation shows that both for the bulk velocity as for the pressure distribution two dimensional flow descriptions yield pressure predictions within an accuracy of 15%. Application of the Reduced Navier Stokes equations are slightly favored since they allow to account for the asymmetry in the geometry.

[2]Main publications: [54, 103, 110].

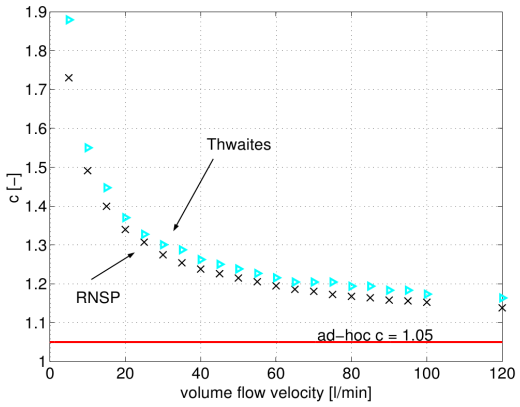

Figure 5.3: Predicted flow separation position.

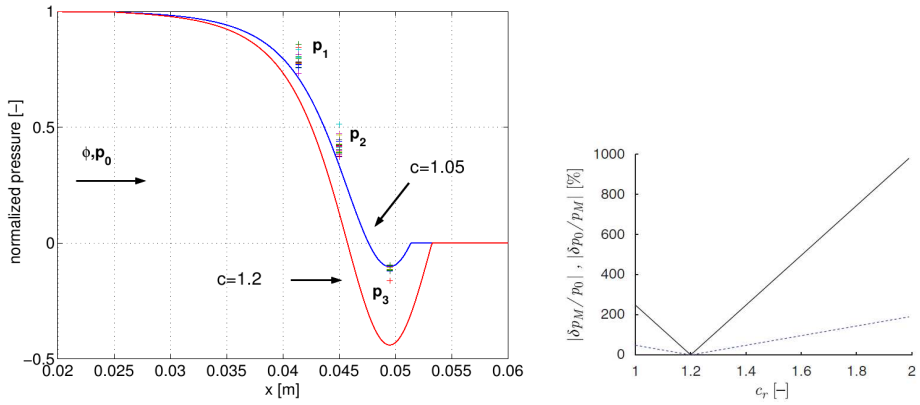

Figure 5.4: Influence of estimation of flow separation on predicted pressure distribution in case of one dimensional flow description: a) example b) Error estimation with upstream p_0 (dashed) or downstream p_M (full) pressure at minimum constriction as known input variable for *ad hoc* assumption $c = 1.2$.

5.3 Constriction shapes: fixed and movable

Simplified[3] simplified quasi one-dimensional flow models and derived inverse models are validated for steady and unsteady flow conditions for the constriction shapes depicted in Fig. 3.11. The aimed models are derived from the irrotational one-dimensional flow equation corrected for viscous effects and flow unsteadiness. The inverse flow models outcome against the direct model input. Next inverse flow models are validated on experimental data obtained for different glottal constriction shapes and flow conditions. The inverse model performance is discussed with respect to the accuracy of the direct model. More advanced models describing accounting for the existence of the boundary layer are assessed.

The following observations are made:

I) Inverse models derived from quasi one-dimensional flow models are formulated in order to retrieve the main

[3]Main publications: [17, 19, 20].

physical variables and models parameters, *i.e.* the upstream pressure, the minimum constriction height or the flow separation coefficient. The accuracy of the inverse models is validated firstly against theoretical simulations obtained with the corresponding direct models and secondly against experimental data. The proposed inverse models allow to retrieve the original direct model input exactly with a minimum of computational effort. Moreover the severe influence of flow separation, wall viscosity and unsteadiness due to wall movement on the model predictions is pointed out for respectively a divergent round constriction shape, small apertures within the order of magnitude of the viscous steady boundary layer thickness and high Strouhal numbers. Experimental validation in both steady and unsteady flow conditions is achieved on rigid replicas with uniform and round constriction shapes in order to study the impact of respectively wall viscosity and flow separation on the inverse model perfomances. Some experimental and model results are illustrated in Fig. 5.5.

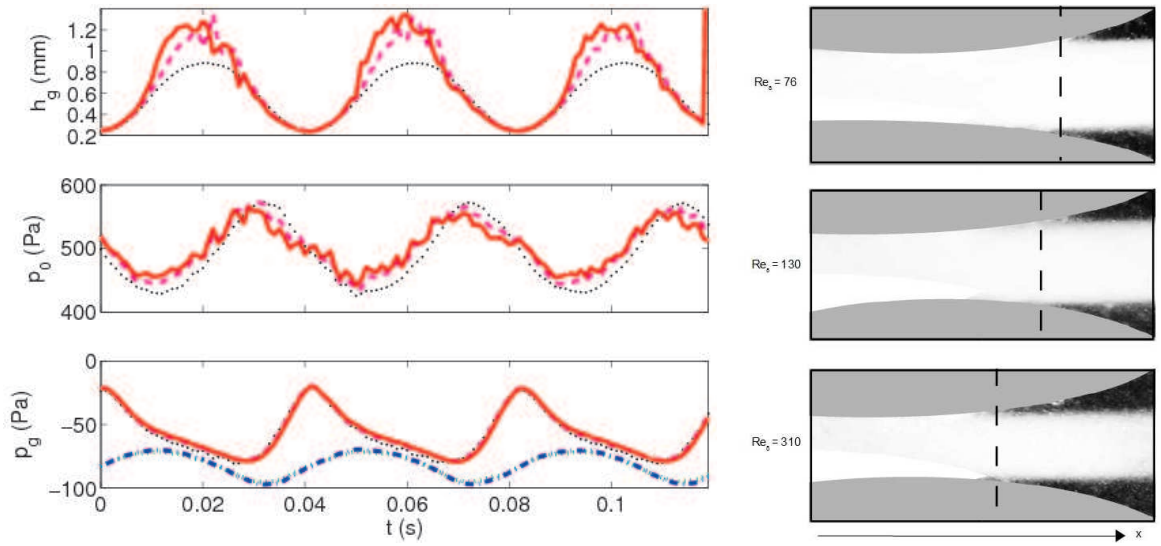

Figure 5.5: a) Measurements (points) and model predictions for the round vocal folds vibrating at 25Hz: (top) minimum constriction height h_g, (middle) upstream pressure p_0 and (bottom) pressure at the minimum constriction height p_g. Predictions are computed with $c_s = 1.08$ and given by the steady Bernoulli (thin dashed line), steady Poiseuille (thin solid line), unsteady Bernoulli (thick solid line) and unsteady Poiseuille (thick dashed line) models. b) Smoke visualisation of the flow separation within the round vocal fold replicas with the minimum constriction height $h_g = 1mm$. The separation positions corresponding to three modified Reynolds numbers, $Re_\delta = Reh_g/L$ with L the length of the constriction, are indicated.

II) It appears that both wall viscosity and the position of flow separation determine the accuracy of the inverse quasi one-dimensional models. A mean prediction accuracy of 20% for the sought physical variables can be achieved for a divergent round constriction shape in case of the inverse models account for wall viscosity and a suitable flow separation coefficient is applied. Remark that the necessity of a corrective term related to viscosity outlines the limitations of the one-dimensional inviscid Bernoulli model. Moreover the predictions errors of the models increase whenever the contribution of the viscosity related term to the estimated quantities decreases. Next the performance of the inverse models is seen to reflect the accuracy of the direct models. Therefore on one hand it seems interesting to include the error sensitivity to input variables in the minimization problem and on the other hand the use of more advanced flow models is motivated. A first intermediate step might be considered in order to validate the value of the separation coefficient as a function of the Reynolds number from more advanced glottal flow models. Comparaison of models with different complexity is shown in Fig. 5.6.

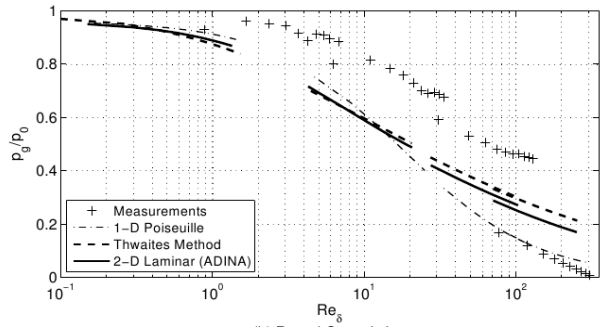

(a)

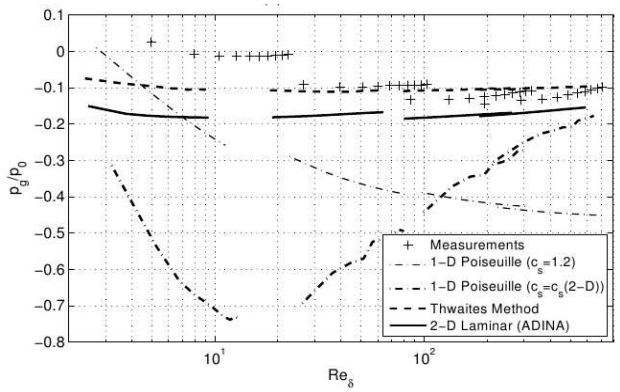

(b)

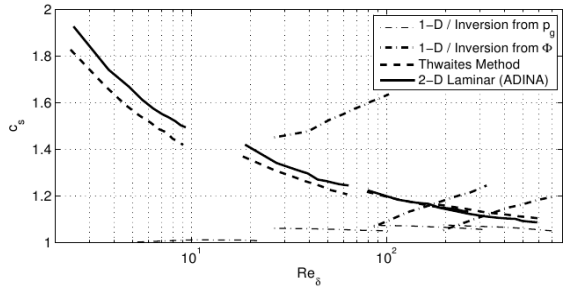

(c)

Figure 5.6: Ratio between the upstream pressure p_0 and the pressure at the minimum constriction height p_g obtained experimentally and simulated a) for the uniform constriction and b) for the round constriction. c) Separation coefficient c_s obtained by inversion with one-dimensional model and simulated by Thwaites and laminar two-dimensional Navier Stokes for the round constriction.

5.4 Rectangular nozzle with 1 gradual and 1 sharp obstacle

A[4] rectangular nozzle with 1 gradual and 1 sharp obstacle is presented in Fig. 3.10 and reminded in Fig. 5.7. In the following it is aimed to validate simple one-dimensional laminar flow models, assumed in Bernoullis equation, corrected by several 'ad-hoc' corrections to describe the influence of vorticity and turbulence on the mean flow. The gap between the upstream gradual and sharp obstacle (between 0 and 81% of the unconstricted channel height) as well as the constriction degree at the sharp obstacle (between 0 and 96% of the unconstricted obstacle) are

[4]Main publications: [101, 109].

systematically varied. In addition, flow conditions are varied so that the range of Reynolds numbers is varied up to $Re_b < 15000$. The flow is characterized by measuring the volume flow rate and performing point pressure measurements at different positions along the replica indicated in Fig. 3.10.

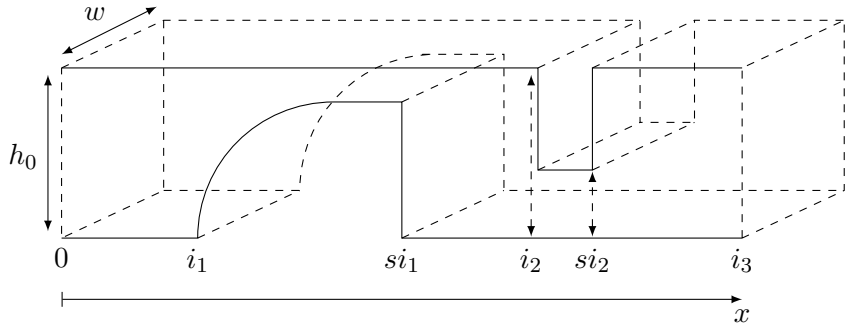

Figure 5.7: Schematic overview of the geometry: rectangular channel with fixed width w characterized by height variation $h(x)$. The unconstricted channel height is denoted h_0 and two constrictions are inserted spanning the intervals $]i_1\ si_1]$ and $]i_2\ si_2]$. The x-axis indicates the main flow direction.

The following observations are made:

I) Point pressure are measured at several streamwise locations and appeared to vary significantly over the range of imposed geometrical gaps. In addition, varying the gap between the upstream gradual and sharp obstacle while maintaining the aperture at the sharp obstacle is seen to influence the pressure at the sharp obstacle. Consequently, besides the aperture at the sharp obstacle aperture, the length of the gap between both obstacles influences the resulting airflow. This is confirmed by fitting the measured pressure drop as function of imposed geometrical parameters since the accuracy of the volume flow rate estimation increases with 40% when the length of the gap between both obstacles is taken into account as well.

II) Measured pressures and volume airflow rates are compared to the outcome of one-dimensional flow models assuming a laminar incompressible irrotational and one-dimensional flow governed by Bernoulli's equation to which corrections are applied for viscosity, sudden geometrical expansion, sudden geometrical constriction and bending. In presence of the upstream gradual obstacle, the accuracy for each set of geometrical parameters expressed as a mean error for all predicted quantities and all imposed upstream pressures yields $< 30\%$. The relevance of additional corrections (resulting in the smallest errors) varies as function of the assessed geometrical parameter set. For very small ($\leq 58\%$) or very large ($\geq 96\%$) constriction degrees at the sharp obstacle, the most accurate model is obtained by accounting for viscosity regardless the separation distance between both obstacles. For intermediate constriction degrees, in the interval $[58\ 96]\%$, narrowing the gap between both constrictions causes the most accurate model to shift from constriction to bending. Therefore, the geometrical parameter corresponding to the gap length, although not explicitly appearing as a parameter in the validated one-dimensional models, does determine the appropriate corrective term for the applied cost function. In addition, it is interesting to note that the best model accuracy is the lowest for constriction degrees at the sharp obstacle ($\approx 60\%$) for which the influence of distance between both obstacles on the measured pressures is most significant. The best model accuracy is shown in Fig. 5.8.

III) Consequently, one-dimensional flow models can be applied to describe the flow through the vocal tract when accounting for the relevant corrections in order to compensate, on geometrical considerations, for the non realistic assumption of a laminar and irrotational flow.

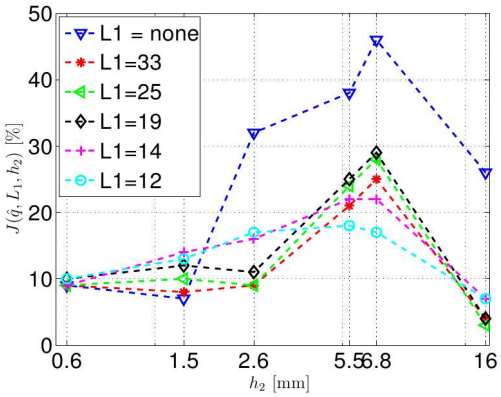

Figure 5.8: Overall best mean model error $J(\hat{q}, L_1, h_2)$ of the models $\hat{q}(L_1, h_2)$ with L_1 denoting the gap length between both obstacles and h_2 the aperture at the sharp obstacle.

5.5 Rectangular nozzle with 1 sharp obstacle

Velocity[5] data are provided downstream an sharp obstacle in a rectangular uniform channel as shown in Fig. 3.9. The inflow is steady and the Re-number is set to $Re = 4000$. The obstruction degree yields 70% and the width-to-height ratio is set to 4 to ensure two-dimensional flow. A comparison of experimental and numerical mean and turbulent velocity data obtained by Large Eddy Simulation (LES) is provided in the near flow field downstream the obstacle from $x = 0$ up to $x/h = 1.5$ where h denotes the aperture. Both the inner and outer layers of the jet issuing from the aperture are sought. The characterisation is inspired on features commonly observed for plane wall jets since a two-layer shear flow can be expected [23, 55, 100].

Experimental as well as numerical flow data for a two-dimensional jet issuing from a sharp constriction for a flow with Reynolds number 4000. In particular the near field is studied since a good characterisation is needed in order to describe sound production due to the interaction of an airflow with the obstacle.

The following observations are made:

I) A first comparison between simulated and experimental velocity features is obtained by quantifying features typically dealt with in studies of a plane wall jet as illustrated in Fig. 5.9. This is motivated since the current problem is basically thought of as a two-layer shear flow consisting of an inner layer (similar to a boundary layer) and an outer layer (similar to a free shear layer) as is the case for a plane wall jet. Nevertheless, the current results, numerical as well as experimental, show that the interaction between the two generic layers leads to a more complex near flow field for which more layers can be distinguished. Therefore, future studies should consider the flow field in more detail; i.e. involving both the near and the fully developed region in order to validate established self-similar models and scaling laws for the plane wall jet.

[5] Main publications: [35, 37, 108].

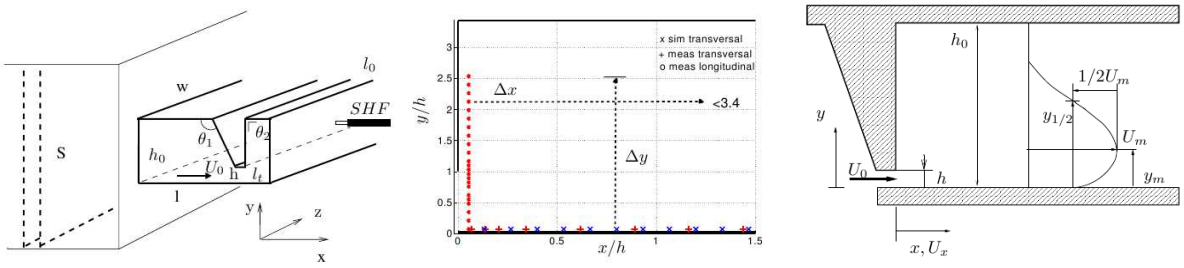

(a) (b)

Figure 5.9: a) Schematic illustration of experimental setup and nozzle with SHF denoting stationary hot film (SHF) anemometry. The main flow direction is indicated by a bold arrow. Initial data stations for transverse ($y < 0.5$mm and Δy =0.1mm) and longitudinal ($x < 0.5$mm $\Delta x = 0.1$mm) profiles gathered downstream the trailing edge of the obstacle, corresponding to $x/h = 0$ and $y/h = 1$, for SHF measurements (transverse $+$, longitudinal $\circ$) are indicated. In addition, transverse profiles taken from simulations ($\times$) for comparison are given as well. b) Nozzle and some major geometrical and flow parameters derived from plane wall jet nomenclature [23]: transverse flow direction y, longitudinal flow component $U_x(x)$ in the main flow direction x indicated by a bold arrow, characteristic velocity at the constriction outlet U_0 at $x \approx 0$, aperture height h , channel height h_0, $y_m(x)$ distance from the wall up to the position of maximum flow velocity $U_m(x)$ in the transversal velocity profile, $y_{1/2}(x)$ distance from the wall up to the outer position where the velocity corresponds to $U_m/2(x)$.

II) From the comparison of the experimental and simulated flow features, illustrated in Fig. 5.10, it is seen that the mean flow fields show the same general tendencies, but differ when considering the quantified features. The main common observations for the mean velocity include: 1) the position of maximum velocity y_m shifts towards the wall for increasing downstream position, 2) the maximum mean velocity U_m increases downstream the constriction, 3) the jet width is seen to decrease for increasing downstream position, 4) as does the ratio of the position of maximum velocity to the outer half width $y_m/y_{1/2}$. Nevertheless, some important differences are observed from the quantified mean velocity features with respect to the structure of the jet: 1) the experimentally observed jet is broadened compared to the numerical jet, 2) the experimental mean velocity exhibits a narrow peak for $y/h \approx 1$, which is absent for the simulated data, 3) the position of maximum velocity is reached for $y/h \approx 1$ on the experimental data, which is larger than for the simulated data and finally 4) the ratio of the position of maximum velocity to the outer half width $y_m/y_{1/2}$ is close to one for the experimental data. The observed differences are the result of increased mean velocity and mean velocity gradients in the vicinity of the teeth edge, i.e. $y/h \approx 1$, for the experimental data compared to the simulated data. Both observations are important considering vorticity. The narrow peak near the obstacle edge, observed on the measured mean velocity profiles, is accompanied with a narrow symmetrical peak in turbulence intensity up to 10%. The observed peak is absent in the simulated flow field, which is laminar in the near field downstream the constriction. It should be noted that although more accurate measurements can be performed, e.g. by using other measurement techniques, the observed differences largely exceed the uncertainty of the velocity measurements and are therefore significant.

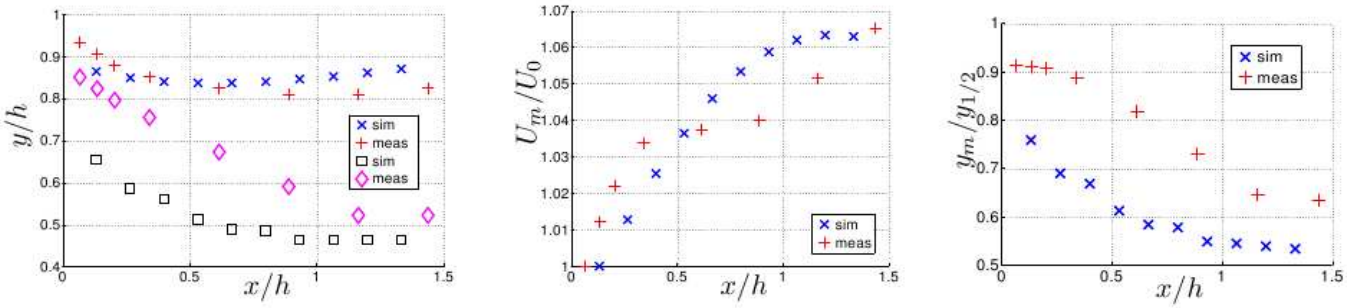

(a) $y_{1/2}(\times, +), y_m(\square, \diamond)$ (b) U_m/U_0 (c) $y_m/y_{1/2}$

Figure 5.10: Measured (meas) and simulated (sim) near field evolution $0 < x/h < 1.5$, for a) position of maximum velocity and outer position of half the maximum velocity $y_{1/2}$ (simulated = $\times$ and measured = $+$) and y_m (simulated = $\square$ and measured = $\diamond$). b) ratio of maximum velocity to characteristic outlet velocity U_m/U_0. c) ratio of positions y_m and $y_{1/2}$, i.e. $y_m/y_{1/2}$.

Chapter 6

Applications to the upper airways

The geometries, flow models and flow characterisation dealt with in the previous chapters are relevant for applications to the upper airways. In the following three examples are given: phonation, fricative production and obstructive sleep apnea.

6.1 Phonation

Phonation[1] or human voiced speech production can be generally represented as a fluid-structure interaction between the airflow coming from the lungs and the vocal folds tissues in the glottis for which a schematic representation is depicted in Fig. 6.1. Consequently, besides a flow model, a mechanical and acoustic model is required as well.

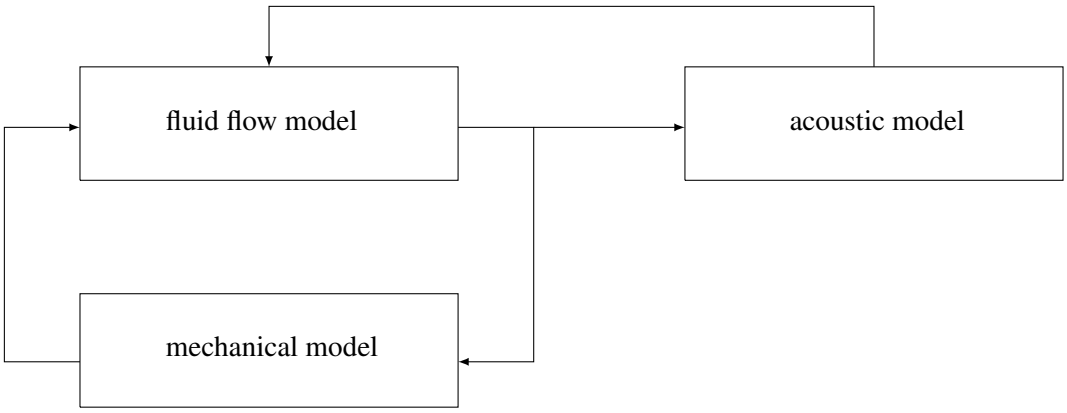

Figure 6.1: Schematic representation of the model approach for speech production.

6.1.1 Theoretical model and stability analysis

The theoretical symmetrical two-mass model is schematically depicted in Fig. 6.2. In the following the model detailed in [61, 83] is briefly outlined and the parameter γ is introduced. Next, the system equations resulting from a

[1] Main publications: [18, 60, 62, 83, 104].

linear stability analysis are derived. Note that the same approach can be applied to a one-mass or delayed one-mass model.

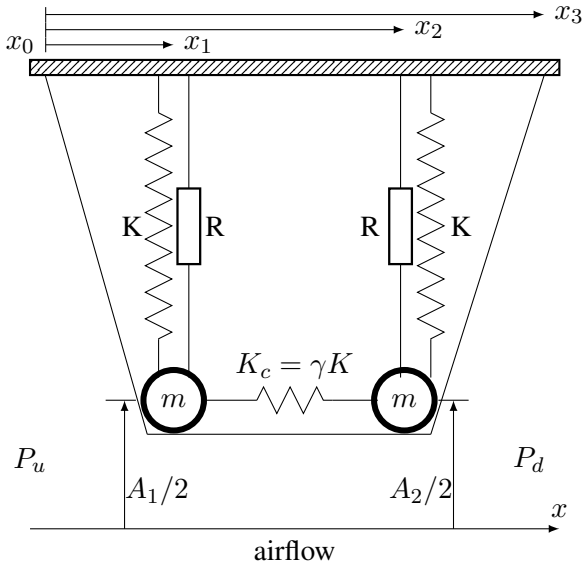

Figure 6.2: Schematic representation of a symmetrical two mass model [61, 83] introducing the parameter γ.

Flow model

The flow through the glottal constriction is described assuming a quasi-steady inviscid and incompressible flow corrected for some viscous effects in case of small glottal apertures and flow separation in the diverging portion of the glottis as $A_s(t) = 1.2 \times \min(A(x,t))$. The pressure distribution $P(x,t)$ and volume flow rate Φ is written as:

$$P(x,t) = P_u - \frac{1}{2}\rho\Phi^2\left(\frac{1}{A^2(x,t)} - \frac{1}{A^2(x_0)}\right) + 12\mu w^2\Phi\int_{x_0}^{x}\frac{dx}{A^3(x,t)}, \qquad \text{if } x < x_s, \tag{6.1}$$

$$P(x,t) = P_d, \qquad \text{if } x \geq x_s, \tag{6.2}$$

with w the uniform width of the glottal replica, μ the dynamic viscosity of air and ρ the density of air, so that

$$\Phi = \frac{12\mu w^2\Phi\int_{x_0}^{x}\frac{dx}{A^3(x,t)} + \sqrt{\left(12\mu w^2\Phi\int_{x_0}^{x}\frac{dx}{A^3(x,t)}\right)^2 + 2(P_u - P_d)\rho\left(1/A_s^2 - 1/A^2(x_0)\right)}}{\rho\left(1/A_s^2 - 1/A^2(x_0)\right)}. \tag{6.3}$$

Mechanical model

Using the notations introduced in Fig. 6.2, the mechanical model is written as two coupled equations:

$$\frac{m}{2}\frac{d^2A_1}{dt^2} + \frac{R}{2}\frac{dA_1}{dt} + \frac{K(1+\gamma)}{2}A_1 - \frac{\gamma K}{2}A_2 = F_1(A_1, A_2, P_u, P_d), \tag{6.4}$$

$$\frac{m}{2}\frac{d^2A_2}{dt^2} + \frac{R}{2}\frac{dA_2}{dt} + \frac{K(1+\gamma)}{2}A_2 - \frac{\gamma K}{2}A_1 = F_2(A_1, A_2, P_u, P_d), \tag{6.5}$$

with $F_{1,2}$ the force exerted by the fluid on the first and second mass respectively. The mechanical equations at equilibrium reduces to:

$$\frac{K(1+\gamma)}{2}\bar{A}_1 - \frac{\gamma K}{2}\bar{A}_2 = F_1(\bar{A}_1, \bar{A}_2, \bar{P}_u, \bar{P}_d = 0), \tag{6.6}$$

$$\frac{K(1+\gamma)}{2}\bar{A}_2 - \frac{\gamma K}{2}\bar{A}_1 = F_2(\bar{A}_1, \bar{A}_2, \bar{P}_u, \bar{P}_d = 0), \tag{6.7}$$

from which the equilibrium positions for a given upstream pressure $\bar{P}_u$ are derived by a fixed point method. Assuming a small perturbation (a_1, a_2, p_u, p_d) of the quantities around the equilibrium values $eq = (\bar{A}_1, \bar{A}_2, \bar{P}_u, \bar{P}_d = 0)$ as:

$$A_1 = \bar{A}_1 + a_1, \qquad A_2 = \bar{A}_2 + a_2, \tag{6.8}$$

$$P_u = \bar{P}_u + p_u, \qquad P_d = \bar{P}_d + p_d, \tag{6.9}$$

results in the following set of equations:

$$\frac{m}{2}\frac{d^2a_1}{dt^2} + \frac{R}{2}\frac{da_1}{dt} + \frac{K(1+\gamma)}{2}a_1 - \frac{\gamma K}{2}a_2 = \left.\frac{\partial F_1}{\partial A_1}\right|_{eq} a_1 + \left.\frac{\partial F_1}{\partial A_2}\right|_{eq} a_2 + \left.\frac{\partial F_1}{\partial P_u}\right|_{eq} p_u + \left.\frac{\partial F_1}{\partial P_d}\right|_{eq} p_d, \tag{6.10}$$

$$\frac{m}{2}\frac{d^2a_2}{dt^2} + \frac{R}{2}\frac{da_2}{dt} + \frac{K(1+\gamma)}{2}a_2 - \frac{\gamma K}{2}a_1 = \left.\frac{\partial F_2}{\partial A_1}\right|_{eq} a_1 + \left.\frac{\partial F_2}{\partial A_2}\right|_{eq} a_2 + \left.\frac{\partial F_2}{\partial P_u}\right|_{eq} p_u + \left.\frac{\partial F_2}{\partial P_d}\right|_{eq} p_d. \tag{6.11}$$

Acoustic model

The acoustic set of equations is given as:

$$\frac{d^2\psi_d}{d^2t} + \frac{\omega_d}{Q_d}\frac{d\psi_d}{dt} + \omega_d^2\psi_d = \frac{Z_d\omega_d}{Q_d}\phi, \tag{6.12}$$

$$\frac{d^2\psi_u}{d^2t} + \frac{\omega_u}{Q_d}\frac{d\psi_u}{dt} + \omega_u^2\psi_u = -\frac{Z_u\omega_u}{Q_u}\phi, \tag{6.13}$$

with $\partial\psi_{u,d}/\partial t = p_{u,d}$ the acoustic pressure and ϕ the unsteady portion of the volume flow velocity downstream the vocal folds, $\omega_{u,d}$ the acoustical resonance pulsation, $Q_{u,d}$ the quality factor and $Z_{u,d}$ the peak value of the acoustical impedance. As for the mechanical equations assuming small variations around equilibrium results in:

$$\frac{d^2\psi_d}{d^2t} + \frac{\omega_d}{Q_d}\frac{d\psi_d}{dt} + \omega_d^2\psi_d = \frac{Z_d\omega_d}{Q_d}\left(\left.\frac{\partial\Phi}{\partial A_1}\right|_{eq} a_1 + \left.\frac{\partial\Phi}{\partial A_2}\right|_{eq} a_2 + \left.\frac{\partial\Phi}{\partial P_u}\right|_{eq} p_u + \left.\frac{\partial\Phi}{\partial P_d}\right|_{eq} p_d\right), \tag{6.14}$$

$$\frac{d^2\psi_u}{d^2t} + \frac{\omega_u}{Q_d}\frac{d\psi_u}{dt} + \omega_u^2\psi_u = -\frac{Z_u\omega_u}{Q_u}\left(\left.\frac{\partial\Phi}{\partial A_1}\right|_{eq} a_1 + \left.\frac{\partial\Phi}{\partial A_2}\right|_{eq} a_2 + \left.\frac{\partial\Phi}{\partial P_u}\right|_{eq} p_u + \left.\frac{\partial\Phi}{\partial P_d}\right|_{eq} p_d\right). \tag{6.15}$$

Consequently, assuming small variations around equilibrium results in a coupled set of equations obtained from (6.10), (6.11), (6.14) and (6.15):

$$m\frac{d^2a_1}{dt^2} + R\frac{da_1}{dt} - 2\frac{\partial F_1}{\partial P_u}\bigg|_{eq}\frac{d\psi_u}{dt} - 2\frac{\partial F_1}{\partial P_d}\bigg|_{eq}\frac{d\psi_d}{dt} + \left(K(1+\gamma) - 2\frac{\partial F_1}{\partial A_1}\bigg|_{eq}\right)a_1 - \left(\gamma K + 2\frac{\partial F_1}{\partial A_2}\bigg|_{eq}\right)a_2 = 0, \tag{6.16}$$

$$m\frac{d^2a_2}{dt^2} + R\frac{da_2}{dt} - 2\frac{\partial F_2}{\partial P_u}\bigg|_{eq}\frac{d\psi_u}{dt} - 2\frac{\partial F_2}{\partial P_d}\bigg|_{eq}\frac{d\psi_d}{dt} - \left(\gamma K + 2\frac{\partial F_2}{\partial A_1}\bigg|_{eq}\right)a_1 + \left(K(1+\gamma) - 2\frac{\partial F_2}{\partial A_2}\bigg|_{eq}\right)a_2 = 0, \tag{6.17}$$

$$\frac{d^2\psi_d}{d^2t} - \frac{Z_d\omega_d}{Q_d}\frac{\partial\Phi}{\partial P_u}\bigg|_{eq}\frac{d\psi_u}{dt} + \left(\frac{\omega_d}{Q_d} - \frac{Z_d\omega_d}{Q_d}\frac{\partial\Phi}{\partial P_d}\bigg|_{eq}\right)\frac{d\psi_d}{dt} - \frac{Z_d\omega_d}{Q_d}\frac{\partial\Phi}{\partial A_1}\bigg|_{eq}a_1 - \frac{Z_d\omega_d}{Q_d}\frac{\partial\Phi}{\partial A_2}\bigg|_{eq}a_2 + \omega_d^2\psi_d = 0, \tag{6.18}$$

$$\frac{d^2\psi_u}{d^2t} + \left(\frac{\omega_u}{Q_d} + \frac{Z_u\omega_u}{Q_u}\frac{\partial\Phi}{\partial P_u}\bigg|_{eq}\right)\frac{d\psi_u}{dt} + \frac{Z_u\omega_u}{Q_u}\frac{\partial\Phi}{\partial P_d}\bigg|_{eq}\frac{d\psi_d}{dt} + \frac{Z_u\omega_u}{Q_u}\frac{\partial\Phi}{\partial A_1}\bigg|_{eq}a_1 + \frac{Z_u\omega_u}{Q_u}\frac{\partial\Phi}{\partial A_2}\bigg|_{eq}a_2 + \omega_u^2\psi_u = 0. \tag{6.19}$$

The system can be expressed in state-space form as

$$\dot{X} = MX \tag{6.20}$$

with $X = [a_1, a_2, \psi_u, \psi_d, da_1/dt, da_2/dt, d\psi_u/dt, d\psi_d/dt]$ and M defined as:

$$M = \left[\begin{array}{cccc|cccc}
0 & 0 & 0 & 0 & 1 & 0 & 0 & 0 \\
0 & 0 & 0 & 0 & 0 & 1 & 0 & 0 \\
0 & 0 & 0 & 0 & 0 & 0 & 1 & 0 \\
0 & 0 & 0 & 0 & 0 & 0 & 0 & 1 \\
\hline
-\frac{K(1+\gamma)-2\frac{\partial F_1}{dA_1}|_{eq}}{m} & \frac{\gamma K+2\frac{\partial F_1}{dA_2}|_{eq}}{m} & 0 & 0 & -\frac{R}{m} & 0 & \frac{2}{m}\frac{\partial F_1}{\partial P_u}|_{eq} & \frac{2}{m}\frac{\partial F_1}{\partial P_d}|_{eq} \\
\frac{\gamma K+2\frac{\partial F_2}{dA_1}|_{eq}}{m} & -\frac{K(1+\gamma)-2\frac{\partial F_2}{dA_2}|_{eq}}{m} & 0 & 0 & 0 & -\frac{R}{m} & \frac{2}{m}\frac{\partial F_2}{\partial P_u}|_{eq} & \frac{2}{m}\frac{\partial F_2}{\partial P_d}|_{eq} \\
\frac{Z_d\omega_d}{Q_d}\frac{\partial\Phi}{\partial A_1}\Big|_{eq} & \frac{Z_d\omega_d}{Q_d}\frac{\partial\Phi}{\partial A_2}\Big|_{eq} & 0 & -\omega_d^2 & 0 & 0 & \frac{Z_d\omega_d}{Q_d}\frac{\partial\Phi}{\partial P_u}\Big|_{eq} & -\left(\frac{\omega_d}{Q_d} - \frac{Z_d\omega_d}{Q_d}\frac{\partial\Phi}{\partial P_d}\Big|_{eq}\right) \\
-\frac{Z_u\omega_u}{Q_u}\frac{\partial\Phi}{\partial A_1}\Big|_{eq} & -\frac{Z_u\omega_u}{Q_u}\frac{\partial\Phi}{\partial A_2}\Big|_{eq} & -\omega_u^2 & 0 & 0 & 0 & -\left(\frac{\omega_u}{Q_d} + \frac{Z_u\omega_u}{Q_u}\frac{\partial\Phi}{\partial P_u}\Big|_{eq}\right) & -\frac{Z_u\omega_u}{Q_u}\frac{\partial\Phi}{\partial P_d}\Big|_{eq}
\end{array}\right]. \tag{6.21}$$

For a known set of initial conditions the system will become instable, corresponding to oscillation onset, in case the real portion of an eigenvalue of M is positive. The corresponding oscillation pulsation is obtained as the imaginary portion of the eigenvalue.

Note that in the foregoing collision is detected following the criterion $h_c = A/w < h_{crit}$ in which case the values of K and R are increased to $K = 4K$ and $R = R + 2\sqrt{Km}$. The fixed collision threshold h_{crit} is set to 0.02 mm.

6.1.2 Example of results

The symmetrical deformable constriction depicted in Fig. 3.16 is used to validate theoretical low-dimensional models. Experimental results establish the influence of independent initial conditions on the observed oscillation onset and offset pressures as well as the oscillation frequency. In a first attempt to include the measured open area in the modelling, commonly used low order models are assessed for which the geometrical input parameter is derived on the measured open area as an averaged aperture. Comparison of measured and modelled onset and offset upstream pressure threshold for auto-oscillation is shown in Fig. 6.3.

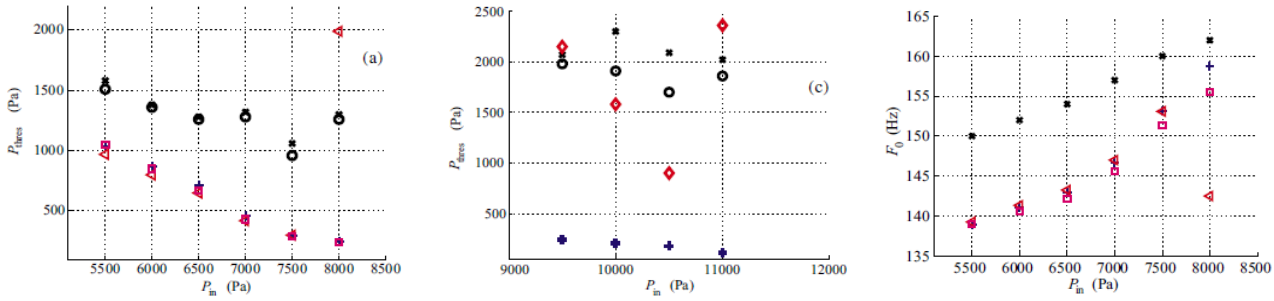

(a) (b) (c)

Figure 6.3: Experimentally observed onset ($\times$), offset ($\circ$) a) modelled P_{thres} for separator 0.0 and b) modelled P_{thres} 1.0 mm and c) modelled F_0: ($+$) two-mass model with $h_{crit} = 0.02$ mm and geometrical h_a^0 mass estimation, ($\triangleleft$) two-mass model with $h_{crit} = 0.5$ mm and geometrical h_a^0 mass estimation, ($\square$) one-mass model with $h_{crit} = 0.02$ mm and geometrical h_a^0 mass estimation, ($\Diamond$) two-mass model with $h_{crit} = 0.02$ mm and mass estimated from the mechanical resonance frequency.

It is seen that the models are capable of predicting the oscillation thresholds and frequencies qualitatively. Quantitative predictions remain difficult for mainly three reasons: 1) the estimation of the model parameter m is critical, 2) the model itself does not accurately describe some crucial phenomena like the contact of the lips or of the vocal folds and 3) an averaged aperture does not take account of the influence of viscosity in case of partial closure of the open area. The influence of the collision model is illustrated in Fig. 6.4.

6.2 Voiceless sound production: fricatives

Research aiming physical modelling of human speech production is mainly concentrated on voiced sound production. Aerodynamic and aeroacoustic principles have been introduced in speech production studies dealing with fricatives since [26]. This pioneering work has been further developed by experimental as well as modeling studies: [4, 44, 52, 90–92]. As a result, the underlying mechanism of fricative sound production is generally described as

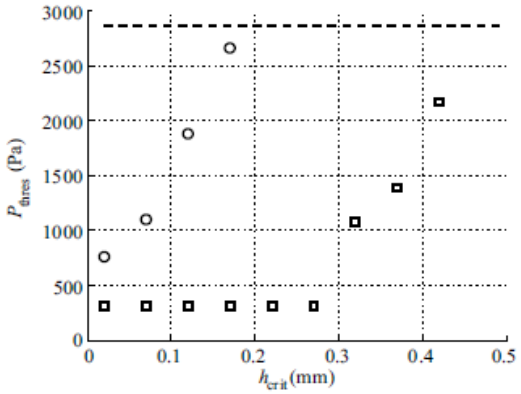

Figure 6.4: Influence of the aperture criterion h_{crit} triggering the application of the collision model on the simulated P_{thres} for features derived from h_a (□) and h_c (○) for separator 0.5 mm and P_{in}=11000 Pa. The dashed line indicates the experimentally observed P_{thres} value.

noise produced due to the interaction of a turbulent jet, issued from a constriction somewhere in the vocal tract, with a downstream wall or obstacle. Consequently, the position and shape of articulators like tongue and teeth determine the generation and development of the jet as well as its downstream interaction with a wall or obstacle as is indeed observed on human speakers [70,81]. It follows that experimental and simulation studies have been performed in order to characterize and quantify the influence of articulators position and shape on the sound produced [72, 77, 89, 90]. Nevertheless, the previous focus on the acoustics of fricative noise production and not on the flow. Therefore, a necessary step to describe unvoiced fricative sound production is to characterise the flow through the vocal tract downstream the glottis, an extensive and systematic validation of flow through the vocal tract downstream the glottis for configurations relevant for unvoiced sound production is lacking as recently pointed out [10, 44]. Therefore, in order to gain insight in the flow development it is necessary 1) to perform a systematic comparison of measurements on simplified mechanical vocal tract models to physical flow models and 2) to gradually increase the complexity of the flow models.

The design of the nozzles outlined in the previous chapters fulfill these requirements so that at term the described characterisation and model validation is likely to contribute to physical modelling and related applications of human fricative speech sound production since:

- **Extended axisymmetrical nozzles:** relatively short extended convergent-divergent diffusers with length-to-diameter ratios $L_t/d < 20$ are considered [74]. Such geometrical configurations, although a crude approximation, are relevant to flow through the human upper airways since: 1) a narrowed upstream passage is present in the upper airways, e.g. at the larynx (glottis) and the lips, or naturally created in the oropharynx during articulation [28, 44, 64, 95] and 2) a typical vocal tract length for a newborn and adult is 7 and 18cm respectively [28, 64, 95]. Further variation of the geometrical length scale L_t, corresponding to varying the extension length is e.g. due to morphology, pathology or articulation during speech production. Since the assessed flow and geometries cover the range relevant to upper airway flow during speech production, initial conditions and in particular initial turbulence levels at the exit of the sought extended nozzles are likely to exhibit important variations depending on the articulator's positions.
- **Rectangular nozzle with 1 sharp obstacle:** the position and geometry of the sharp obstacle matches the physiological data of an upper incisor. As such the nozzle represents a single upper incisor inserted in a channel and allows to study the flow around a teeth-shape obstacle.

- **Rectangular nozzle with 1 gradual and 1 sharp obstacle:** the current nozzle accounts for jet formation upstream a sharp obstacle representing the tongue and teeth articulators. As such the flow data observed and modelled for this nozzle geometry is mostly related to real life fricative production. Moreover observed sound spectra do allow to reproduce typical spectra associated with human fricative production.

6.3 Obstructive sleep apnea

Obstructive[2] sleep apnea can be generally represented as a fluid-structure interaction between the airflow coming from the lungs and the upper airway tissues for which a schematic representation is depicted in Fig. 6.5. Consequently, a flow and mechanical model are required to account for OSA.

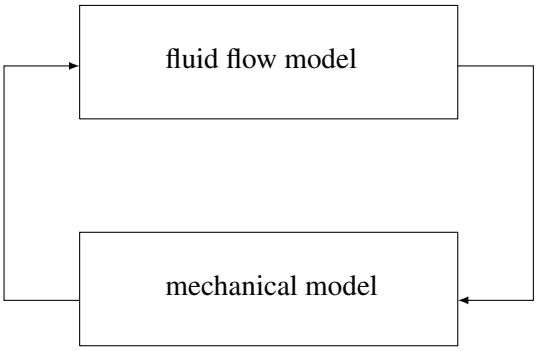

Figure 6.5: Schematic representation of the model approach for obstructive sleep apnea.

Experimental and modelled resuls on the asymmetrical deformable replica presented in Fig. 3.13 are compared in Fig 6.6. The experimental results correspond to a collapse of about 25 % corresponding to the 'in-vitro' reproduction of a hypopnea syndrome due to the negative pressure forces along the constriction. In absence of flow the minimum constriction coincides with the position of the pressure tap p_1 at the centre of half cylinder. Increasing the upstream pressure p_0 results in negative pressures at all pressure taps, i.e. at the support centre 0, 8 and 16 mm further downstream. Further increasing the pressure results in a further decrease 16 mm after the centre while at the centre a positive pressure is retrieved. Therefore the curves confirm the displacement of the minimum constriction in the flow direction prevailed in the dye experiment illustrated in Figure 3.15.

The overall model prediction agrees well with the experimental data. In all cases the error remains well below 20 % considered as the upper limit for worst case error. Replica reopening is observed in Fig. 6.6(b) for experimental data 1. This behaviour can not be predicted by the applied model due to the assumption of quasi-steadiness. Reopening is associated with the onset of instabilities retrieved in e.g. snoring. The flow limitation due to the wall displacement characterising the collapse is for the examples showed in Figure 6.6 yield 49.9 and 69.6 %, respectively. The percentages of flow limitation are comparable to 'in-vivo' order of magnitudes of about 50 % in case of hypopnea. So both the theoretical as the experimental model are suitable to study at partial collapse and in particular the presented experimental model is therefore a valuable alternative to the classical Starling resistor experiment. The theoretical model is not capable to predict total collapse since among others a collision model is not taken into account. The contact during the collision influences e.g. the onset of instabilities to a large extent.

[2]Main publications: [15, 16, 17, 103].

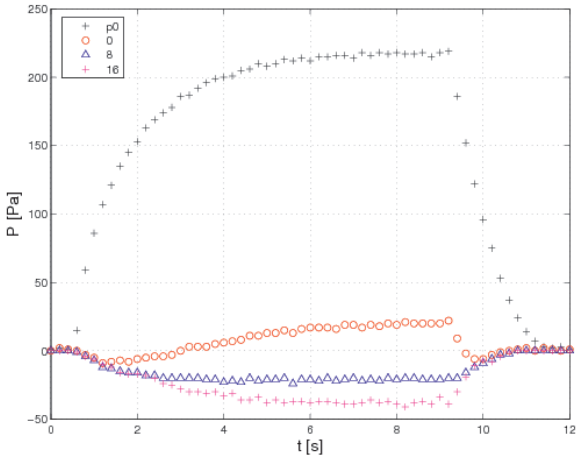

(a) ΔP=200Pa, P_{in}=200Pa

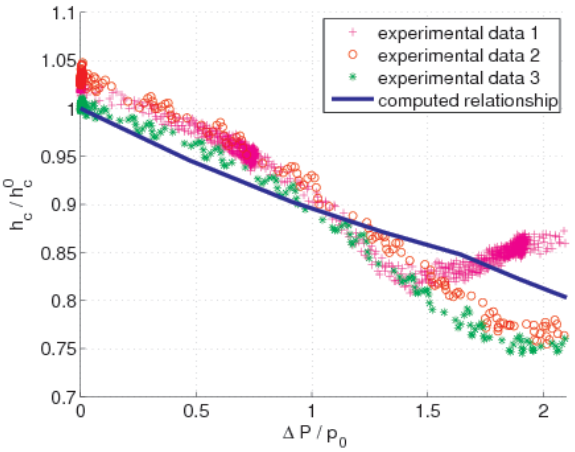

(b) ΔP=200Pa, h_c^0=1.2mm, P_{in}=200Pa

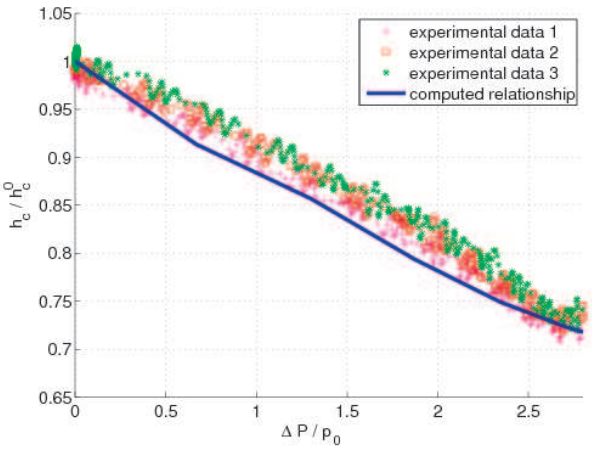

(c) ΔP=290Pa, h_c^0=0.87mm, P_{in}=400Pa

Figure 6.6: a) Measured pressures P(t) for the deformable replica Pa for the upstream pressure (p_0) and for the pressure taps at the positions indicated in Fig. 6.6 at the middle of the metal cylinder 0 (○), 8 (△) and 16 (+) mm downstream. b,c) Simulation of a hypopnea illustrating measured (+,○,∗) and predicted (full line) centre height h_c as a function of upstream pressure.

Chapter 7

Conclusion and perspectives

7.1 Conclusion

The current document reports on the study of moderate Reynolds number flow in a range $100 - 10^4$ relevant to phenomena associated with the human upper airways. Besides practical relevance the range of Reynolds numbers is less studied in literature so that flow data are missing. In addition, since the human upper airways geometry is very different from typical well designed nozzle geometries mostly dealt with in literature, the study of flow through a-typical nozzles is needed. Since in particular in speech production most research deals with phonation the study of nozzles suitable to mimic the e.g. the oral tract articulators are limited. The current document therefore aims to contribute to the study of moderate Reynolds number flow through a-typical nozzles. Nevertheless, it is in no way aimed to study flow through real human upper airway geometries. Instead some severe simplifications are made.

Different aspects of moderate Reynolds number flow are dealt with:

7.1.1 Experiments

From an experimental point of view a contribution is made to the development of experimental setups for flow measurement and flow visualisation as well as aeroacoustic measurements. As such a simple setup and algorithm for hot film/wire calibration in the range of low and moderate flow velocities is presented in order to obtain quantitative information of the velocity field at a given position. In addition to quantitative point measure by anemometry, a simple setup for flow visualisation is used enabling a qualitative overall view of the flow field. Next, a setup for acoustic measurements is realised aiming firstly to isolate from external noises due to either the flow facility, colleagues or outdoor noises and secondly aiming to provide an approximation of free field conditions for sound registration.

Several simplified rigid mechanical replicas are presented starting from a tube or channel and gradually increasing the complexity of the replica under study by introducing 1 or 2 obstacles with a sharp or more gradual constriction. Consequently the presented mechanical replicas allow to study the flow at the exit of axisymmetrical tubes or two dimensional channels for which among others the inlet geometry can be varied, the length of the carrier tube or channel, the shape of the obstacle and the length of the constricted region. A step motor can be mounted to some of the rigid obstacles so that the influence of wall movement on the flow can be studied.

In addition to rigid obstacles, two deformable replicas are outlined for which the initial aperture can be varied by adding shims. As such, the replicas are in particular suitable to study the influence of initial conditions on the flow-structure interaction.

7.1.2 Characterisation of jet development

Jet development at the exit of the axisymmetrical tubes and two-dimensional channels are characterised from hot-wire anemometry and smoke visualisation. Transverse and longitudinal velocity profiles are quantified in order to characterise main statistical features of the mean and fluctuating flow field. As such a start is made to take into account turbulent flow in relation to simplified mechanical replicas of limited dimension and volume flow rate. In addition, the coherent structures associated with the onset to turbulence are visualised and characterised by means of simple image processing techniques.

In case of axisymmetrical tubes in particular the influence of the inlet geometry and tube extension length on the measured velocity profiles is sought for different Reynolds numbers. Both the mean and turbulence level of the initial profile at the tube outlet is observed to depend on both the Reynolds number as the tube extension length for fixed diameter. From the longitudinal centerline velocity profiles the mean velocity decay is characterised by parameters well studied in literature such as the decay constant, virtual origin and potential core length. It is observed that values for Reynolds numbers approximating 1.1×10^4 correspond to values reported in literature for the decay constant and potential core length although not for the virtual origin. In addition, the experimentally measured jet spreading rate is used to estimate the turbulence viscosity. Smoke visualisation mainly confirms the hot-wire measurements and makes their interpretation easier.

Vortex dynamics in the near field downstream an asymmetrical rectangular nozzle is studied in the range $100 < Re < 1100$ based on rectangular vortex dynamics extracted from smoke visualisation images. As for the axisymmetrical nozzles the influence of the bulk Reynolds number on the spatial and temporal evolution of counterclockwise and clockwise vortices is assessed. Vortex streamwise stretching is observed to decrease with Reynolds number and the shedding frequency is seen to increase linearly with Reynolds number from which the Strouhal number can be estimated.

7.1.3 Validation of flow models

Different flow models with increasing complexity are validated on experimental data mainly resulting from point pressure measurements and hot wire anemometry.

Simplified direct and inverse one-dimensional flow models are seen to qualitative model the flow behaviour for two-dimensional constrictions of different geometries. Nevertheless, the position of flow separation remains a crucial aspect and an unphysical position is needed for an accurate description of the pressure distribution. Boundary layer solutions are seen to strongly improve this drawback of one-dimensional flow modeling. Nevertheless, it is obvious that the laminar flow models does not account for turbulence development and as such their use is limited downstream a constriction for which turbulence develops in the shear layers.

The performance of adding loss terms to one-dimensional laminar flow models based on geometrical considerations in order to predict the mean flow in a channel with 2 obstacles is seen to result in a qualitative prediction. Nevertheless more complex models accounting for turbulence are required in order to increase the accuracy and to estimate the fluctuating portion of the flow field. A start is made by simulating the flow through a two-dimensional channel with one obstacle by large eddy simulation. Although a good qualitative agreement is obtained between the simulated and measured flow field in the near field downstream the obstacle the quantitative dismatch remains.

7.1.4 Application to the upper airways

The previous described research is applied to phenomena associated with the upper airways such as speech production and Obstructive Sleep Apnea (OSA).

At first application to a linear stability analysis of phonation is presented using the one-dimensional flow models. Particular attention is given to the influence of mechanical model parameters and their relationship with experimentally measurable quantities. Next, since turbulence is taken into account at term the current research is likely to contribute to human fricative production.

Finally, an application is presented to obstructive sleep apnea.

7.2 Perspectives

Perspectives of the presented research are many.

It is obvious that despite the multitude of studied nozzle geometries and mechanical replicas it concerns mostly axisymmetrical or two-dimensional nozzles so that it is of obvious interest to vary the geometry. Moreover most of presented research deals with rigid nozzle geometries which does not account for a viscous layer adjactant to the wall. Obviously the presence of such a layer influences the boundary layer development and an extension to two-phase fluid is in particular interesting for pathological applications such as asthma.

It is aimed to apply the estimated turbulence viscosity in a simple turbulent flow model at least in order to predict the flow along the centerline. Moreover the current experimental data need to be studied from the point of view of flow stability in order to extent modeling of the flow. Besides an estimation of the fluctuating properties of the flow, the next step is obvious aero-acoustic modeling in order to estimate the sound production as well as to consider the influence of acoustics on the flow development and vice-versa.

Finally, although a great effort is made with respect to the development of the experimental setup, increasing the measurement accuracy requires further development. It is aimed to obtain quantitative velocity information from Particle Image Velocimetry. In addition, it is aimed to extent the anemometry measurements to more than one velocity component. Moreover mostly steady flow is studied. Obviously the experimental setup needs to be developed in order to account for unsteady flow. From the point of view of acoustic measurements it is of interest to consider

microphone antennes in order firstly to obtain information on the directivity and secondly on the source region.

Furthermore, mainly flow modelling is discussed although more complex mechanical modeling is needed in order to describe complex fluid-structure interaction phenomena such as phonation, osa or lung sounds.

Bibliography

[1] *Elastomeres datasheet*, 2010.

[2] P. 0'Neill, J. Soria, and D. Honnery. The stability of low reynolds number round jets. *Exp*, 36:473–483, 2004.

[3] A. Abdel-Rahman, S. Al-Fahed, and W. Chakroun. The near-field characteristics of circular jets at low Reynolds numbers. *Mechanics Research Communications*, 23:313–324, 1996.

[4] S. Adachi and K. Honda. CFD approach to fricative sound sources. In *Proc. 6th International Seminar on Speech Production*, pages 1–4, Sydney, Australia, 2003.

[5] Inc ADINA R&D. *A.D.I.N.A. Theory and Modeling Guide Volume III: ADINA CFD & FSI.* Inc, Watertown, MA, U.S.A., 2006.

[6] R. Antonia and Q. Zhao. Effect of initial conditions on a circular jet. *Exp. Fluids*, 31:319–323, 2001.

[7] G.K. Batchelor. *An introduction to fluid dynamics*. Cambridge Mathematical Library, 2000.

[8] J.H. Bell and R.D. Mehta. Contraction design for small low-speed wind tunnels. *NASA STI/Recon Technical Report N*, 89:22, 1988.

[9] R.D. Blevins. *Applied Fluid Dynamics Handbook*. Krieger publishing company, Malabar, 1992.

[10] D. Bodony. The prediction and understanding of jet noise. *Center for Turbulence Research Annual Research Briefs*, pages 367–377, 2005.

[11] B. Boersma, G. Brethouwer, and F. Nieuwstadt. A numerical investigation on the effect of the inflow conditions on the self-similar region of a round jet. *Phys. Fluids*, 10:899–909, 1998.

[12] H.H. Bruun. *Hot-wire anemometry*. Oxford Science Publications, New York, 1995.

[13] P. Burattini, R. Antonia, S. Rajagopalan, and M. Stephens. Effect of initial conditions on the near-field development of a round jet. *Exp. Fluids*, 37:56–64, 2004.

[14] T. Cebeci and J. Cousteix. *Modeling and computation of boundary-layer flows*. Springer, 2005.

[15] F. Chouly. *Modélisation physique des voies aériennes supérieures pour le syndrome d'apnées obstructives du sommeil*. PhD thesis, 2005.

[16] F. Chouly, A. Van Hirtum, P.Y. Lagrée, X. Pelorson, and Y. Payan. Modelling the human pharyngeal airway: validation of numerical simulations using in-vitro experiments. *Medical & Biological Engineering & Computing*, 47:49–58, 2009.

[17] J. Cisonni. *Modélisation et inversion d'un système complexe de production de signaux acoustiques: application à la voix et aux pathologies*. PhD thesis, Grenoble, France, 2008.

[18] J. Cisonni, A. Van Hirtum, X. Pelorson, and J. Lucero. The influence of geometrical and mechanical input parameters on theoretical models of phonation. *Acta Acustica*, 2:291–302, 2011.

[19] J. Cisonni, A. Van Hirtum, X. Pelorson, and J. Willems. Theoretical simulation and experimental validation of inverse quasi one-dimensional steady and unsteady glottal flow models. *J. Acoust. Soc. Am.*, 124:535–545, 2008.

[20] J. Cisonni, A. Van Hirtum, Luo X.Y., and X. Pelorson. Experimental validation of quasi one-dimensional and two-dimensional steady glottal flow models. *Med. Biol. Eng. Comput.*, 48:903–910, 2010.

[21] R.C. Deo, J. Mi, and G.J. Nathan. The influence of Reynolds number on a plane jet. *Physics of Fluids*, 20, 2008.

[22] M. Deverge, X. Pelorson, C. Vilain, P. Lagree, F. Chentouf, J. Willems, and A. Hirschberg. Influence of collision on the flow through in-vitro rigid models of the vocal folds. *J. Acoust. Soc. Am.*, 114(6):1–9, 2003.

[23] J. Eriksson, R. Karlsson, and J. Person. An experimental study of a two-dimensional plane turbulent wall jet. *Experiments in Fluids*, 20:50–60, 1998.

[24] O. Estienne. *Etude aéraulique et aéroacoustique de la production de consonnes fricatives par modèle physique*. PhD thesis, Grenoble University, 2010.

[25] F. Fang. A design method for contractions with square end sections. *J. Fluid Eng.*, 119:454–458, 1997.

[26] G. Fant. *The acoustic theory of speech production*. Mouton, The Hague, 1960. p.328.

[27] H. Fellouah, C.G. Ball, and A. Pollard. Reynolds number effects within the development region of a turbulent round free jet. *International Journal of Heat and Mass Transfer*, 52:3943–3954, 2009.

[28] W. Fitch and J. Giedd. Morphology and development of the human vocal tract: A study using magnetic resonance imaging. *J. Acoust. Soc. Am.*, 106:1511–1522, 1999.

[29] Y. Fujiso and A. Van Hirtum. Evaluation des performances d'une chambre d'isolation acoustique destinee a la validation experimentale de production de parole. In *Proc. RJCP*, page 4, Grenoble, France, 2011.

[30] Y. Fujiso, B. Wu, X. Grandchamp, and A. Van Hirtum. Caracterisation d'un convergent axisymetrique. In *Proc. 20ieme CFM*, page 6 (Accepted), Besancon, France, 2011.

[31] W. George. The decay of homogeneous isotropic turbulence. *Phys. Fluids A*, 4:1492–1509, 1992.

[32] W.K. George. *Recent advances in Turbulence*, chapter The self-preservation of turbulent flows and its relation to initial conditions and coherent structures, pages 39–73. Hemisphere, New York, 1989.

[33] W.K. George, H. Abrahamsson, J. Eriksson, R.I. Karlsson, L. Löfdahl, and M. Wosnik. A similarity theory for the turbulent plane wall jet without external streaming. *J. Fluid Mech.*, 425:367–411, 2000.

[34] M. Germano, U. Piomelli, P. Moin, and W. Cabot. A dynamic subgrid-scale eddy viscosity model. *Phys Fluids A*, 3:1760–1765, 1991.

[35] X. Grandchamp. *Modélisation physique des écoulements turbulents appliquées aux voies aériennes supérieures chez l'humain*. PhD thesis, Grenoble Universities, 2009.

[36] X. Grandchamp, Y. Fujiso, and A. Van Hirtum. Jet rond en aval d'une contraction brusque. In *Proc. 20ieme CFM*, page 6 (Accepted), Besancon, France, 2011.

[37] X. Grandchamp, A. Van Hirtum, K. Nozaki, J. Cisonni, X. Pelorson, and S. Shimojo. Visualisation of moderate reynolds number flow through a tooth-shaped nozzle. In *Proc. 20th Int. Conf. of Acoustics (ICA)*, page 6, Sydney, Australia, 2010.

[38] X. Grandchamp, A. Van Hirtum, and X. Pelorson. Experimental validation of simplified free jet turbulence models applied to the vocal tract. In *Proc. Int. Conf. on Acoustics (ICA)*, page 6, Madrid, Spain, September 2007.

[39] X. Grandchamp, A. Van Hirtum, and X. Pelorson. Hot film/wire calibration for low to moderate flow velocities. *Meas. Sci. Technol.*, 21:115402, 2010.

[40] F.F. Grinstein. Vortex dynamics and entrainment in rectangular free jets. *J. Fluids Mech.*, 437:69–101, 2001.

[41] E. Gutmark and C.M. Ho. Preferred modes and the spreading rates of jets. *Phys. Fluids*, 26:2932–2938, 1983.

[42] P.T. Harsha. Free turbulent mixing: a critical evaluation of theory and experiment. Technical report, 1971.

[43] C. Ho and P. Huerre. Perturbed free shear layers. *Annu. Rev. Fluid Mech.*, 16:365–424, 1984.

[44] M.S. Howe and R.S. McGowan. Aeroacoustics of [s]. *Proc. R. Soc. A*, 461:1005–1028, 2005.

[45] F. Hsiao, Y. Lim, and J. Huang. On the near-field flow structure and mode behaviors for the right-angle and sharp-edged orifice plane jet. *Experimental Thermal and Fluid Science*, In press:1–8, 2010.

[46] H.H. Hubbard, editor. *Aeroacoustics of flight vehicles*. Acoustical Society of America, 1995.

[47] A. Hussain and M. Zedan. Effects of the initial condition on the axisymmetric free shear layer: Effects of the initial momentum thickness. *Phys. Fluids*, 20:1100–1112, 1978.

[48] H. Hussein, S. Capp, and W. George. Velocity measurements in a high Reynolds number momentum conserving axisymmetric turbulent jet. *J. Fluid Mech.*, 258:31–75, 1994.

[49] S. Iio, K. Takahashi, Y. Haneda, and T. Ikeda. Flow visualisation of vortex structure in a pulsed rectangular jet. *J. of Visualization*, 11:125–132, 2008.

[50] A. Johnstone, M. Uddin, and A. Pollard. Calibration of hot-wire probes using non-uniform mean velocity profiles. *Exp. Fluids*, 39:1432–1114, 2005.

[51] N.L. Kachhara, P.L. Wilcox, and J.L. Livesey. A theoretical and experimental investigation of flow through short axisymmetric contractions. In *Proc. 5th Australian Conf. on Hydraulics and Fluid Mechanics*, pages 82–89, Christchurch, New Zealand, 1974.

[52] M. Krane. Aeroacoustic production of low-frequency unvoiced speech sounds. *J. Acoust. Soc. Am.*, 118(1):410–427, 2005.

[53] S.J. Kwon and I.W. Seo. Reynolds number effects on the behavior of a non-buoyant round jet. *Exp. Fluids*, 38:801–812, 2005.

[54] P.Y. Lagrée, A. Van Hirtum, and X. Pelorson. Asymmetrical effects in a 2D stenosis. *European Journal of Mechanics B/Fluids*, 26:83–92, 2007.

[55] B.E. Launder and W. Rodi. The turbulent wall jet - measurements and modeling. *Annu. Rev. Fluid Mech.*, 15:429–459, 1983.

[56] T. Lee and R. Budwig. Two improved methods for low-speed hot-wire calibration. *Meas. Sci. Technol.*, 2:643–646, 1991.

[57] M. Lesieur, O. Métais, and P. Comte. *Large-Eddy Simulations of Turbulence*. Cambridge University Press, New York, 2005.

[58] D. Lilly. A proposed modification of the Germano subgrid-scale closure method. *Physics of Fluids*, 4:633–635, 1992.

[59] S.C. Ling and C.A. Wan. Decay of isotropic turbulence generated by a mechanically agitated grid. *Phys. Fluids*, 15:1363, 1972.

[60] I. Lopez, A. Hirschberg, A. Van Hirtum, N. Ruty, and X. Pelorson. Physical modeling of buzzing artificial lips: The effect of acoustical feedback. *Acta Acustica*, 92(6):1047–1059, 2006.

[61] N. Lous, G. Hofmans, N. Veldhuis, and A. Hirschberg. A symmetrical two-mass vocal-fold model coupled to vocal tract and trachea, with application to prosthesis design. *Acta Acustica*, 84:1135–1150, 1998.

[62] J. Lucero, A. Van Hirtum, N. Ruty, J. Cisonni, and X. Pelorson. Validation of theoretical models of phonation threshold pressure with data from a vocal fold mechanical replica. *J. Acoust. Soc. Am.*, 125:632–635, 2009.

[63] T.G. Malmstrom, A.T. Kirkpatrick, B. Christensen, and K.D. Knappmiller. Centreline velocity decay measurements in low-velocity axisymmetric jets. *J. Fluid Mech.*, 246:363–377, 1997.

[64] R. McGowan. Perception of synthetic vowel exemplars of 4 year old children and estimation of their corresponding vocal tract shapes. *J. Acoust. Soc. Am.*, 120:2850–2858, 2006.

[65] R.D. Metha and P. Bradshaw. Design rules for small low speed wind tunnels. *The Aeronautical J. of the Royal Aeronautical Society*, 18:443–449, 1979.

[66] J. Mi, R.C. Deo, and G.J. Nathan. Characterization of turbulent jets from high-aspect-ratio rectangular nozzles. *Physics of Fluids*, 17:4, 2005.

[67] J. Mi, P. Kalt, G. Nathan, and C. Wong. PIV measurements of a turbulent jet issuing from round sharp-edged plate. *Exp. Fluids*, 42:625–637, 2007.

[68] J. Mi, D. Nobes, and G. Nathan. Influence of jet exit conditions on the passive scalar field of an axisymmetric free jet. *J. Fluid Mech.*, 432:91–125, 2001.

[69] T. Morel. Comprehensive design of axisymmetric wind tunnel contractions. *J. Fluid Eng.*, 97:225–233, 1975.

[70] S. Narayanan, A. Alwan, and K. Haker. An articulatory study of fricative consonants using magnetic resonance imaging. *J. Acoust. Soc. Am.*, 98:1325–1347, 1995.

[71] H.B. Nottage. Report on ventilation jets in room air distribution. Technical report, Case Inst. of Technology, Cleveland, Ohio, 1951.

[72] K. Nozaki, T. Akiyama, S. Shimojo, S. Maeda, and H. Tamagawa. Integration of computational fluid dynamics and computational aero acoustics on grid for dental applications. In *Proc.18th IEEE Symposium on Computer-Based Medical Systems*, pages 517–522, Ann Arbor, MI, USA, 2005.

[73] N. Panchapakesan and J. Lumley. Turbulence measurements in axisymmetric jets of air and helium. part 1. air jet. *J. Fluid Mech.*, 246:197–224, 1993.

[74] X. Pelorson, A. Hirschberg, R. Van Hasselt, A. Wijnands, and Y. Auregan. Theoretical and experimental study of quasisteady-flow separation within the glottis during phonation. Application to a modified two-mass model. *J. Acoust. Soc. Am.*, 96:3416–3431, 1994.

[75] W. Pitts. Reynolds number effects on the mixing behavior of axisymmetric turbulent jets. *Exp. Fluids*, 11:1432–1114, 1991.

[76] W. Quinn. Upstream nozzle shaping effects on near field flow in round turbulent free jets. *Eur. J. Mech. B/Fluids*, 25:279–301, 2006.

[77] G. Ramsay. The influence of constriction geometry on sound generation in fricative consonants. In *Proc. Acoustics08*, pages 1–4, Paris, France, 2008.

[78] G. Romano and R. Antonia. Longitudinal and transverse structure functions in a turbulent round jet: effect of initial conditions and Reynolds number. *J. Fluid Mech.*, 436:231–248, 2001.

[79] L. Rosenhead. *Laminar boundary layers*. Dover, 1963.

[80] T.D Rossing. *The science of sound*. Moore & Wheeler, 2002.

[81] C. Runte, M. Lawerino, D. Dirksen, F. Bollmann, A. Lamprecht-Dinnesen, and E. Seifert. The influence of maxillary central incisor position in complete dentures on /s/ sound production. *The journal of prosthetic dentistry*, 85:485–495, 2001.

[82] S. Russ and P. Strykowski. Turbulent structure and entrainment in heated jets: The effect of initial conditions. *Phys. Fluids*, 5:3216–3225, 1993.

[83] N. Ruty, X. Pelorson, A. Van Hirtum, I. Lopez, and A. Hirschberg. An in-vitro setup to test the relevance and the accuracy of low-order vocal folds models. *J. Acoust. Soc. Am.*, 121(1):479–490, 2007.

[84] P. Sagaut and M. Germano. *Large Eddy Simulation for Incompressible Flows*. Spring Verslag, New York, 2005.

[85] H. Sato. The stability and transition of a two-dimensional jet. *J. Fluid Mechanics*, 7:53–80, 1960.

[86] J.C. Sautet and D. Stepowski. Dynamic behavior of variable-density, turbulent jets in their near development fields. *Phys. Fluids*, 7(2):2796–2806, 1995.

[87] H. Schlichting and K. Gersten. *Boundary layer theory*. Springer Verlag, Berlin, 2000.

[88] M.E. Schneider and R.J. Goldstein. Laser doppler measurement of turbulence parameters in a two-dimensional plane wall jet. *Phys. Fluids*, 6:3116–3129, 1994.

[89] C. Shadle. The effect of geometry on source mechanisms of fricative consonants. *J. Phonetics*, 19:409–424, 1991.

[90] C.H. Shadle. *The acoustics of fricative consonants*. PhD thesis, Dept. Electrical Engineering. Massachusetts Institute of Technology, 1985.

[91] C.H. Shadle, M. Berezina1, M. Proctor, and K. Iskarous. Mechanical models of fricatives based on MRI-derived vocal tract shapes. In *Proc. 8th International Seminar on Speech Production*, pages 417–420, Strasbourg, France, 2008.

[92] D. Sinder. *Speech Synthesis Using an Aeroacoustic Fricative Model*. PhD thesis, 1999.

[93] K.M. Smith and J.C. Dutton. A procedure for turbulent structure convection velocity measurements using time-correlated images. *Exp. in Fluids*, 27:244–250, 1999.

[94] I.J. Sobey. *Introduction to interactive boundary layer theory*. Oxford University Press, New York, 2005.

[95] K Stevens. *Acoustic Phonetics*. MIT Press, London, 1998.

[96] K. Stewartson. D'Alembert's Paradox. *SIAM review*, 23:308–343, 1981.

[97] B. Thwaites. On the momentum equation in laminar boundary-layer flow. a new method of uniparametric calculation. Technical Report 2587, Rep. Memor. aero. Res. Coun., Lond., 1947.

[98] B. Thwaites. Approximate calculations of laminar boundary layers. *Aeronautical Quarterly*, 1:245–280, 1949.

[99] V. Todde, P.G. Spazzini, and M. Sandberg. Experimental analysis of low-reynolds number free jets: Evolution along the jet centerline and reynolds number effects. *Exp. Fluids*, 47:279–294, 2009.

[100] A. Townsend. *The structure of turbulent shear flow*. Cambridge University Press, UK, 1999.

[101] A. Van Hirtum. Flow through simplified vocal tract geometries. In *Proc. CFA10 - 10th French Congress of Acoustics*, page 6, Lyon, France, 2010.

[102] A. Van Hirtum, F. Chouly, P.Y. Lagrée, J.R. Paoli, Y. Payan, and X. Pelorson. *When a fluid-structure interaction keeps you awake: a physical approach to Obstructive Sleep Apnea. In New Sleep Apnea Syndrome Research*. Nova, New York, 2007.

[103] A. Van Hirtum, J. Cisonni, and X. Pelorson. On quasi-steady laminar flow separation in the upper airways. *Communications in Numerical Methods in Engineering*, 25:447–461, 2009.

[104] A. Van Hirtum, J. Cisonni, N. Ruty, X. Pelorson, I. Lopez, and F. van Uittert. Experimental validation of some issues in lip and vocal fold physical models. *Acta Acustica*, 93(2):314–323, 2007.

[105] A. Van Hirtum and Fujiso. Insulation room for aero-acoustic experiments at moderate reynolds and low mach numbers. *Applied Acoustics*, In revision, 2011.

[106] A. Van Hirtum, X. Grandchamp, and J. Cisonni. Near field vortex dynamics downstream an asymmetrical nozzle. In preparation, 2011.

[107] A. Van Hirtum, X. Grandchamp, and X. Pelorson. Moderate Reynolds number axisymmetric jet development downstream an extended conical diffuser: influence of extension length. *Eur. J. Mech - B/FLUIDS*, 28:753–760, 2009.

[108] A. Van Hirtum, X. Grandchamp, X. Pelorson, K. Nozaki, and S. Shimojo. LES and 'in-vitro' experimental validation fo flow around a teeth-shaped obstacle. *Int. J. of Applied Mechanics*, 2:265–279, 2010.

[109] A. Van Hirtum, X. Pelorson, O. Estienne, and H. Bailliet. Experimental validation of flow models for a rigid vocal tract replica. *J. Acoust. Soc. Am.*, In revision, 2011.

[110] A. Van Hirtum, X. Pelorson, and P.Y. Lagrée. In vitro validation of some flow assumptions for the prediction of the pressure distribution during obstructive sleep apnoea. *Med. Biol. Eng. Comput.*, 43:162–171, 2005.

[111] F.M. White. *Viscous fluid flow*. McGraw-Hill, New York, 1991.

[112] C.D. Winant and F.K. Browand. Vortex pairing: the mechanism of turbulent mixing-layer growth at moderate reynolds number. *J. Fluid Mech.*, 63:237–255, 1974.

[113] Champagne F. Wygnanski, I. and B. Marasli. On the large scale structures in two-dimensional, small-deficit, turbulent wakes. *J. Fluid Mech.*, 168:31–71, 1986.

[114] I. Wygnanski and H.E. Fiedler. Some measurements in the self preserving jet. *J. Fluid Mech.*, 38:577–612, 1969.

[115] G. Xu and R. Antonia. Effect of different initial conditions on a turbulent round free jet. *Exp. Fluids*, 33:677–683, 2002.

[116] Y. Yeh, H. Hsu, C. Chiang, and F. Hsiao. Vortical structure evolutions and spreading characteristics of a plane jet flow under anti-symmetric long-wave excitation. *Experimental Thermal and Fluid Science*, 33:630–641, 2009.

[117] Z. Yue and T.G. Malmström. A simple method for low-speed hot-wire anemometer calibration. *Meas. Sci. Technol.*, 9:1506–1510, 1998.

Part II

Administrative summary